



Ternary $\text{Co}^{\text{III}}\text{O}_\text{V}\text{Cu}$ sites trigger Co-utilization of endogenous electron donor-acceptor for sustainable removal of refractory low-carbon fatty amines in Fenton-like system

Qin Dai ^{a,1}, Guangfei Yu ^{a,1}, Juanjuan Qi ^a, Yanan Wang ^a, Lei Xing ^c, Yihao Wang ^a, Zhijie Zhang ^a, Xiaolin Zhong ^a, Zhimo Fang ^a, Penghui Du ^d, Lai Lyu ^{b,*}, Lidong Wang ^{a,*}

^a MOE Key Laboratory of Resources and Environmental Systems Optimization, College of Environmental Science and Engineering, North China Electric Power University, Beijing, 102206, P. R. China

^b Institute of Environmental Research at Greater Bay Area; Key Laboratory for Water Quality and Conservation of the Pearl River Delta, Ministry of Education, Guangzhou University, Guangzhou 510006, P. R. China

^c State Key Joint Laboratory of Environment Simulation and Pollution Control, School of Environment, Tsinghua University, Beijing 100084, P.R. China

^d School of Environmental Science and Engineering, Southern University of Science and Technology, Shenzhen, Guangdong 518055, P. R. China



ARTICLE INFO

Keywords:
Oxidant utilization efficiency
Ternary $\text{Co}^{\text{III}}\text{O}_\text{V}\text{Cu}$ sites
Dimethylamine
 O_2 activation
Fenton-like reaction

ABSTRACT

Herein, we fabricated $\text{CoCu-0.25-O}_\text{V}$ with ternary $\text{Co}^{\text{III}}\text{O}_\text{V}\text{Cu}$ sites through simple co-precipitation to achieve effective co-utilization of organics and dissolved oxygen (DO) as endogenous electron donor-acceptor in Fenton-like system. Around 100% of dimethylamine (DMA) min within 30 is removed. The involved kinetics (0.22 min^{-1}) and oxidant utilization efficiency (22.5%) are higher than controls with binary sites. Multi-scaled characterizations and theoretical calculations reveal that electron-polarized $\text{Co}^{\text{III}}\text{O}_\text{V}\text{Cu}$ sites facilitate co-activation of DMA and DO as electron donor-acceptor through increasing d-band center and lowering work function of catalyst. Meanwhile, ternary sites favor ${}^1\text{O}_2$ and SO_4^{2-} generation, and shorten the migration distance of active species to pollutant, thus achieving excellent dual performance improvements. Semi-quantitative results of ESR indicate that DO activation and peroxymonosulfate (PMS) oxidation contribute about three-fourths and one-fourth to ${}^1\text{O}_2$ production, respectively. This contribution provides a new and sustainable strategy for high-efficiency and oxidant-saving removal of refractory pollutants in the environment.

1. Introduction

In recent years, low-carbon fatty amines (LCFAs, $\text{C}_1\sim\text{C}_3$)-containing wastewater discharged from various chemical and industrial production processes, has received increasing attention.^[1,2] Such LCFAs could pose a threat to the water environment due to their strong polarity and potential carcinogenicity, and easily evaporate from water into the atmosphere resulting from their high volatility and further as the main precursors of ozone and $\text{PM}_{2.5}$. In particular, as corrosive and foul-smelling pollutants, even a low concentration of LCFAs would cause a direct serious threat to materials and human health.^[3-5] Different from common benzene-containing unsaturated organics, saturated LCFAs, e.g., monomethylamine (MA), dimethylamine (DMA) and trimethylamine (TMA) feature with simple molecular structure, small

molecular van der Waals volume, strong polarity and water solubility, high bond dissociation energy (e.g., $\sim 365 \text{ kJ/mol}$ of N-H , $\sim 355 \text{ kJ/mol}$ of C-N and $\sim 392 \text{ kJ/mol}$ of C-H for DMA), electron-deficient state and exhibit resistance to biodegradation.^[6] These characteristics make such organics abatement one of the most challenging issues in the field of environmental remediation. As the environmental discharge and emission standards are getting increasingly strict, it is an urgent demand to develop efficient and affordable technologies for *in-situ* degradation and even mineralization of refractory LCFAs in the aqueous phase.

Peroxymonosulfate (PMS)-based Fenton-like heterogeneous system holds a great potential to crack and even mineralize the aqueous LCFAs, since it has exhibited efficient removal performance on various organics in water solution through producing a variety of highly reactive oxygen species (ROSSs) including SO_4^{2-} , ${}^{\bullet}\text{OH}$, and ${}^1\text{O}_2$ et al.^[7,8] Generally,

* Corresponding authors.

E-mail addresses: lyulai@gzhu.edu.cn (L. Lyu), wld@ncepu.edu.cn (L. Wang).

¹ These authors contributed equally to this work.

PMS-based heterogeneous system, e.g., the typical Co-based Fenton-like process, relies on PMS acting as both electron donor (**Pathway I**)^[9,10] and acceptor (**Pathway II**)^[10–12] for the generation of ROSSs to attack organics^[13].

Pathway I PMS as electron donor (i.e., reductant):



Pathway II PMS as electron acceptor (i.e., oxidant):



However, this type of activation process (Eqs. 1–6) inevitably causes a large consumption of PMS especially dealing with small polar molecules such as DMA, i.e., it encounters the issue of low PMS utilization efficiency ($\eta = \Delta[\text{pollutant}]/\Delta[\text{oxidant}]$, which was defined as the mole number of contaminant degradation per PMS consumed)^[14,15]. This not only leads to the increased cost of industrial treatment, but also brings serious secondary pollution such as water acidification, residual sulfate, and metal ion leaching. Undoubtedly, these problems seriously violate the principle of sustainable development^[13].

To address the issues, co-activation of endogenous LCFA and dissolved O₂ (DO) molecules in wastewater to replace PMS as electron donors and acceptors and to facilitate ROSSs generation at the same time is a very promising strategy. The co-utilization of endogenous electron donor-acceptors not only reduces the consumption of PMS, but also synchronously accelerates pollutant removal through multiple pathways (i.e., self-oxidation and ROSSs attacking)^[16,17]. To achieve this goal, the key challenge is to develop multi-site catalysts that can simultaneously activate the specific three reactants (LCFA, DO, and PMS). Gratifyingly, previous studies have shown that Cu site is able to trigger pollutants with electron-donating groups (e.g., -NH₂ and -OH) as electron donors, since they form a more stable Cu(I)-pollutant complex^[18] due to Cu's electron orbital configuration (3d¹⁰ 4 s¹)^[15,18]. The presence of oxygen vacancy (O_v) on catalyst can effectively activate O₂ molecules as electron acceptors to produce ¹O₂, which is because O_v with abundant localized electrons is capable of strengthening the interaction between O₂ and oxide surfaces, facilitating the interfacial charge transfer^[19]. Further, Co site has been widely reported to be superior active sites to other transition metals for adsorption and activation of PMS because of the specific 3d band structure of Co(II)^[19]. Inspired by these three aspects, the fine design of a microenvironment on catalyst containing ternary Co^{...}O_v^{...}Cu sites is expected to trigger the co-utilization of LCFA and DO as the endogenous electron donor-acceptor to replace the consumption of PMS and maintain PMS activity participated in the reactions. More importantly, the fabricated asymmetric Co^{...}O_v^{...}Cu sites could further promote the adsorption and activation of interfacial reactants due to the uniform electronic distribution caused by the O_v linked with two different metals^[20,21]. Also, the design of such three sites close to each other should effectively shorten the migration distance of short-lived ROSSs to pollutants, thus improving the degradation of pollutants in theory. Based on these, multifunctional Co^{...}O_v^{...}Cu sites hold a high potential to achieve the excellent removal of refractory LCFA with a satisfactory PMS utilization rate. Nevertheless, to best of our knowledge, there has been no relevant report and the involved mechanism needs to be further revealed.

Herein, we have prepared a composite catalyst β -Co(OH)₂/γ-Cu₂(OH)₃Cl (CoCu-0.25-O_v) with Co^{...}O_v^{...}Cu trifunctional sites through simple co-precipitation, and DMA is used as a model pollutant

for catalytic performance evaluation in PMS-based Fenton-like system. The resultant catalyst with ternary Co^{...}O_v^{...}Cu site indeed successfully realizes the co-usage of endogenous DMA and DO to replace PMS as the role of electron donor and acceptor, respectively, and further promotes the production of major active species ¹O₂ and SO₄²⁻. As a result, compared with two controls with binary sites (i.e., Co^{...}O_v and Cu^{...}O_v) and other commercial catalysts (e.g., Co₃O₄, Co(OH)₂, CuO, Cu(OH)₂ and CuCl₂), the admirable improvements of catalytic activity (reaction kinetics) and PMS utilization efficiency are achieved on CoCu-0.25-O_v catalyst. Quenching experiments, electron spin-resonance spectrometer (ESR) capture experiments, *in-situ* Fourier transform infrared spectroscopy (FT-IR), and density functional theory (DFT) theoretical calculations were performed collectively to identify the role of electron donor and acceptor. Further, the mechanism for the enhanced catalytic performances governed by the ternary Co^{...}O_v^{...}Cu sites is revealed in depth. Additionally, the effects of various influencing factors in wastewater on catalytic activity and the universality to different amine contaminants were investigated. After the identification of the products, the toxicity and volatility of the intermediates and the primary economic evaluation of our reaction system were further evaluated. Overall, this work breaks through the limitation of high consumption caused by PMS usually as the exclusive electron donor and acceptor and provides a new idea for high-performance and oxidant-saving environmental remediation based on the substitution of endogenous electron donor-receptor, which was triggered by synergies between well-designed O_v-linked multifunctional sites.

2. Experimental section

2.1. Materials and reagents

CoCu-0.25-O_v, individual Co(OH)₂-O_v and Cu₂(OH)₃Cl-O_v catalysts were synthesized through a simple co-precipitation method. Taking CoCu-0.25-O_v as an example, 20 mmol CuCl₂•2 H₂O and 5 mmol CoCl₂•6 H₂O were dissolved in 200 mL deionized water, followed by dropwise addition of mixed NaOH/Na₂CO₃ ([NaOH] = 0.35 mol/L, [Na₂CO₃] = 0.15 mol/L) to adjust the pH value to 10 under vigorous magnetic stirring (600 r.p.m). The mixture was stirred for 30 min at room temperature and subsequently aged at 65 °C for 12 h under a static state. The resulting power was washed with deionized water and ethanol at least 5 times to remove excessive metal salts as well as to ensure the pH was unchanged. The catalyst was dried at 70 °C for 24 h and then CoCu-0.25-O_v was obtained after milling. Likely, the individual Co(OH)₂-O_v and Cu₂(OH)₃Cl-O_v were prepared under identical conditions in the absence of CuCl₂•2 H₂O or CoCl₂•6 H₂O.

All involved chemicals and characterizations methods including high-resolution transmission electron microscopy (HR-TEM), scanning electron microscope (SEM), X-ray powder diffraction (XRD), surface area measurement, X-ray photoelectron spectroscopy (XPS), *in-situ* solid and liquid ESR, FT-IR, and inductively coupled plasma optical emission spectrometry (ICP-OES) are presented in SI.

2.2. Procedures and analysis

The catalytic activities of the prepared catalysts were evaluated by the degradation of DMA under ambient conditions. Typically, 60 mg of catalyst and 100 mL of DMA solution (5 ppm) were mixed in a glass beaker and mechanically stirred for 30 min until the adsorption-desorption equilibrium was achieved. Then, the reaction was started with the addition of 2 mL of PMS (0.3 M) under continuous stirring (400 r.p.m) throughout the experiment. 2 mL of suspension sample was collected and filtered by a 0.22 μm filter hydrophobic membrane and followed by being quenched using 100 μL of Na₂S₂O₃ (0.1 M) immediately. The concentration of DMA after being derived by chloroformic acid 9-fluorenylmethyl ester (FMOC-Cl) was detected on a high-performance liquid chromatography (HPLC, LC3100, Anhui Wanyi

Science and Technology Co., Ltd, China) equipped with a C18 reversed-phase column (4.6 × 250 mm) and a UV detector (detection wavelength was 265 nm).^[3] The remaining PMS was determined by a KI method on UV-visible spectroscopy.^[22] Radical quenching experiments were conducted during the DMA degradation experiment. 100 mM tertiary butyl alcohol (TBA), 100 mM ethanol (EtOH) and 10 mM furfuryl alcohol (FFA) were used to quench $\cdot\text{OH}$, $\text{SO}_4^{\cdot-}$ and O_2^{\cdot} , respectively. Total organic carbon (TOC, mg/L) was determined using a TOC analyzer (5000 A, Shimadzu, Japan). The intermediate products were identified by ion chromatography (IC, CIC-D100, China, Qingdao Shenghan Chromatograph Technology Co., Ltd) and HPLC.

For solid ESR, we have characterized four samples including CoCu-0.25-O_v, CoCu-0.25-O_v/DMA, CoCu-0.25-O_v/PMS, and CoCu-0.25-O_v/DMA/PMS. The four solids were obtained by filtration after the reaction under the same conditions as the catalytic evaluation and followed by natural drying. Then the obtained samples were measured on the low-temperature ESR at 77 K. For liquid ESR, the signals of O_2^{\cdot} , $\text{SO}_4^{\cdot-}$ and $\text{HO}_2^{\cdot}/\text{O}_2^{\cdot-}$ in the corresponding reaction systems were detected, in which 2, 2, 6, 6-tetramethylpiperidine-1-oxyl (TEMP) was used as the spin trapping agent for O_2^{\cdot} and 5,5-dimethyl-1-pyrroline N-oxide (DMPO) was employed as the spin trapping agent for $\text{SO}_4^{\cdot-}/\text{OH}^{\cdot-}$ and $\text{HO}_2^{\cdot}/\text{O}_2^{\cdot-}$ on ESR. Typically, 0.05 g of catalyst and 150 μL of PMS (0.3 M) were added to 0.8 mL of pure solution ($\text{SO}_4^{\cdot-}/\text{OH}^{\cdot-}$ / O_2^{\cdot} detection in aqueous solution and $\text{HO}_2^{\cdot}/\text{O}_2^{\cdot-}$ detection in methanol solution). After the sample was shaken and mixed thoroughly, 100 μL of TEMP (100 mM) or DMP (100 mM) was added. The suspension continued to be shaken for 2 min and drawn into a capillary for detection.

2.3. DFT calculations

Density functional theory (DFT) calculations were performed using a plane-wave basis set with the projector augmented wave (PAW) method as implemented in the Vienna ab-initio simulation package (VASP).^[23] The Perdew-Burke-Ernzerhof (PBE) functional for the exchange-correlation term was used for all calculations. The energy cutoff for the plane wave basis set is set to be 520 eV. The convergence accuracy of the total energy between the two electronic steps is 10^{-6} eV for self-consistent field calculations, and all atoms are allowed to fully relax until the residual force per atom is less than 0.02 eV \AA^{-1} for structural optimization. For the catalyst structure design, a supercell ($4 \times 4 \times 1$) of [001]-oriented $\beta\text{-Co(OH)}_2$ single-layer had been constructed by periodically repeating the five atomic layers along the [001] direction of the unit cell.^[24] Each $\beta\text{-Co(OH)}_2$ single-layer model was separated by a vacuum region of 20 \AA . The Brillouin zone is sampled by a ($3 \times 3 \times 1$) Γ -center k-point mesh. Besides, spin-polarization is included in all computations, and the DFT-D3 method of van der Waals (vdW) correction is adopted to accurately evaluate the interactions between molecules and catalyst surface. The charge population is calculated using Bader charge analysis.^[25] The O_vs formation energy is calculated by $E_{\text{Ov}} = E_{\text{Ov-slab}} - E_{\text{slab}} + 1/2 E_{\text{O}_2}$, in which E_{slab} is the total electronic energy of a pristine slab, $E_{\text{Ov-slab}}$ is the total energy of the slab with surface O_v, and E_{O_2} is the VASP-sol calculated molecular energy of O₂ in the atmosphere. The work function (Φ) is defined as $\Phi = E - E_{\text{F}}$, where E and E_{F} are the energy of vacuum level and the Fermi level, respectively.^[23] The adsorption energy is defined as $\Delta E_{\text{ads}} = E_{\text{total}} - E_{\text{catalyst}} - E_{\text{adsorbate}}$, where E_{total} , E_{catalyst} , and $E_{\text{adsorbate}}$ correspond to the energy of the catalyst/adsorbate complex, catalyst and isolated adsorbate (DMA, O₂ and PMS), respectively. The electron density difference is calculated via $\Delta\rho = \rho_{\text{total}} - \rho_{\text{catalyst}} - \rho_{\text{adsorbate}}$, where ρ_{total} , $\rho_{\text{substrate}}$, and $\rho_{\text{PMS/DMA}}$ are the electron distribution of catalyst/PMS complex, catalyst and isolated adsorbate (DMA and PMS), respectively.

3. Results and discussion

3.1. Characterization for interactive lattice substitution

Fig. 1a shows the facile co-precipitation process for the preparation of CoCu-0.25-O_v. Solution B containing NaOH and Na₂CO₃ was drop-wise added into solution A containing CoCl₂ and CuCl₂ at a mole ratio of 0.25: 1 until the pH reached 10 under vigorous magnetic stirring. After the aging process, CoCl₂ and CuCl₂ were integrated into the CoCu-0.25-O_v. Co(OH)₂-O_v and Cu₂(OH)₃Cl-O_v as two control materials were also prepared under identical conditions without the addition of CuCl₂ or CoCl₂ for comparison. The XRD patterns show that the obtained CoCu-0.25-O_v presents main diffraction peaks at 16.21°, 32.36°, 39.73°, 50.13°, 53.56°, which are indexed as (011), (210), (220), (230) and (322) crystal planes (**Fig. 1b**). These diffraction peaks are also observed on the individual $\gamma\text{-Cu}_2(\text{OH})_3\text{Cl-O}_v$ (PDF# 86-1391), but not on $\beta\text{-Co(OH)}_2\text{-O}_v$ (PDF# 00-014-0117)^[26,27], indicating the dominant position of Cu₂(OH)₃Cl-O_v species. Compared to the two individual catalysts, in the CoCu-0.25-O_v, some peaks disappear ($2\theta = 35.50^\circ$, 38.51° in Cu₂(OH)₃Cl-O_v), some peaks shift ($2\theta = 16.18^\circ$, 32.32°, 39.78°, 50.11° and 53.52° in Cu₂(OH)₃Cl-O_v and $2\theta = 47.09^\circ$ and 59.39° in Co(OH)₂-O_v) and some peaks become much broader. These phenomena are caused by the change of unit cell parameters, indicating that Co and Cu have mutual lattice substitution, which results from their similar ionic radius (Co²⁺ 0.74 \AA , Co³⁺ 0.63 \AA , Cu²⁺ 0.73 \AA and Cu⁺ 0.77 \AA). Meanwhile, the apparent decrease in the intensity and increase in peak width of CoCu-0.25-O_v relative to controls implies more poor crystal properties. This suggests that lattice substitution leads to an increase in lattice structure disorder.

Brunauer, Emmett and Teller (BET) analysis illustrates that the specific surface area (SSA) and pore volume of CoCu-0.25-O_v are 84.9 m^2/g and 0.4 cm^3/g , respectively (inset in **Fig. 1c**). These two values are larger than 62 m^2/g and 0.22 cm^3/g , calculated from the physical mixing of Co(OH)₂-O_v (214.5 m^2/g and 0.7 cm^3/g) and Cu₂(OH)₃Cl-O_v (24.0 m^2/g and 0.1 cm^3/g). This illustrated that the structure of CoCu-0.25-O_v is different from the mix of Co(OH)₂-O_v and Cu₂(OH)₃Cl-O_v. For the pore size distribution, CoCu-0.25-O_v is dominated by mesopore and macropore (**Fig. 1c-d**). The wider distribution and new pore sizes (~21.6, ~34.3 and ~54.4 nm) are observed in CoCu-0.25-O_v relative to the mesoporous Co(OH)₂-O_v (~9.3 and ~14.7 nm) and Cu₂(OH)₃Cl-O_v (~27.2, ~40.0, ~68.5 and ~86.2 nm). This verifies that the different porous structures of the obtained composite. SEM results of CoCu-0.25-O_v further support this conclusion by exhibiting fluffier and more porous morphology compared with Co(OH)₂-O_v and Cu₂(OH)₃Cl-O_v alone (**Fig. S1**).

As shown in the TEM images (**Fig. 1e**), the composite is formed by the Cu₂(OH)₃Cl-O_v nanoparticles (~24 nm) buried in the rod-like Co(OH)₂-O_v (width in ~5 nm and length in ~26 nm, more details can be found in the descriptions along with **Figs. S2-3**). The energy dispersive spectroscopy (EDS) line-scanning profiles in **Fig. 1g** indicate the composite catalyst consists of Co, O, Cu and Cl four elements, and Co, Cu and O are always positively correlated, validating the successful interactive lattice doping of Cu and Co. HRTEM images of CoCu-0.25-O_v display that clear crystal lattice fringes corresponding to the (210), (220) and (322) crystal plane of the Cu₂(OH)₃Cl-O_v and (011) crystal plane of the Co(OH)₂-O_v are observed (**Fig. 1f**). Notably, these lattice fringe spacings are slightly different from the pure Co(OH)₂-O_v and Cu₂(OH)₃Cl-O_v (**Figs. S2-3**). These alterations are attributed to the change of cell structure induced by the lattice doping of Co and Cu, in accordance with the slight XRD peak shifts. Moreover, the lattice fringes became disorder in comparison with the two control materials, which could be assigned to the generation of O_v, since the release of structural oxygen atom leads to poor crystal properties.^[29]

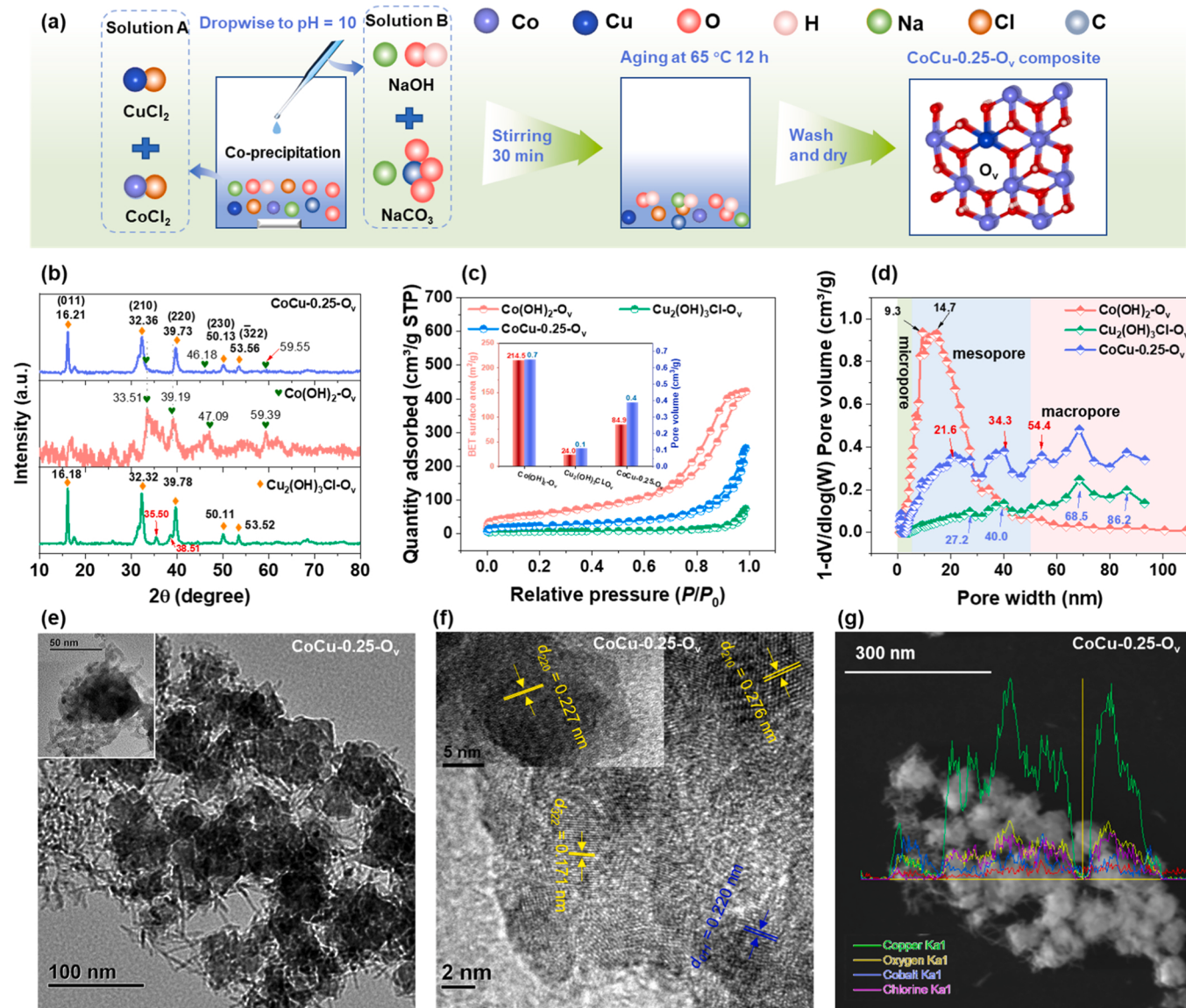


Fig. 1. (a) Illustration of the preparation of CoCu-0.25-O_v composites. (b) XRD patterns. (c) N₂ absorption/desorption isotherms (inset: SSA and pore volume) and (d) pore distributions of three materials. (e) TEM images, (f) HRTEM images, and (g) EDS line-scanning elemental profiles of CoCu-0.25-O_v.

3.2. Formation of ternary Co^{···}O_v^{···}Cu sites induced by interactive lattice substitutions

XPS verifies the co-existence of Co, Cu, O, and Cl elements in CoCu-0.25-O_v (Fig. S4), agreeing well with the EDS results. Specifically, XPS peaks of Cu 2p3/2 observed at 934.25 eV and 935.52 eV are corresponded to Cu(I) and Cu(II) species, respectively, confirmed by the spin-orbital splitting of 19.69 eV and 19.35 eV between the Cu 2p3/2 and Cu 2p1/2 accordingly (Fig. 2a).^[10,15,18,30] It is noted that the atom ratio of Cu(I)/Cu(II) (0.91:1), calculated by the peak areas of Cu(I) and Cu(II), is higher than that of Cu₂(OH)₃Cl-O_v (0.51:1). Cu LMM Auger electron spectroscopies (AES) also present a similar increased trend in the atom ratio of Cu(I)/Cu(II) in CoCu-0.25-O_v, where peak at 574.88 eV corroborates the presence of Cu(I) (Fig. S5).^[30] For the Co 2p XPS deconvolution results of CoCu-0.25-O_v (Fig. 2b), two dominant peaks positioned at about 780.0 eV and 781.09 eV are assigned to the 2p3/2 of Co(III) and Co(II) species, respectively.^[31] The atom ratio of Co(III)/Co(II) (0.29:1) is increased compared to that of solo Co(OH)₂-O_v (0.21:1). Above results clarify that the electrons migrate from Co to Cu because of the greater electronegativity of Cu,^[28] resulting in the

non-uniform distribution of electrons and the formation of electron-poor and electron-rich domains.^[16,32,33] This polarized distribution of electrons on the CoCu-0.25-O_v surface would render a change in the potential distribution, which is ready to be excited, leading to elevated catalytic performance.^[16,34] Furthermore, the appearance of nonequivalent substitution of Cu-Co sites induces the formation of O_v.^[16] The formation of more low-valence state metals in CoCu-0.25-O_v supports the O_v production, since the resulting O_v after oxygen atoms escape could produce extra electrons in the surrounding metal atoms, which lowers the valence state of the metal atoms. The O 1 s XPS spectra are further used to analyze the electronic structure of O species. As shown in Fig. 2c, the O 1 s peak of CoCu-0.25-O_v could be fitted into three characteristic peaks of lattice oxygen (~529.94 eV), hydroxy species (-OH, ~531.51 eV), and O_v (~532.74 eV).^[35] The proportion of O_v in CoCu-0.25-O_v is increased to 19.9% compared with the Co(OH)₂-O_v (Co^{···}O_v, O_v adjacent to Co atoms, 13.9%, Fig. S5b) and Cu₂(OH)₃Cl-O_v (Cu^{···}O_v, 8.3%), confirming that the production of new O_v which is attributed to the nonequivalent substitution of Cu-Co sites.^[16] To reveal the local coordination environment of newly formed O_v, we analyze the content of -OH in the materials, because the three

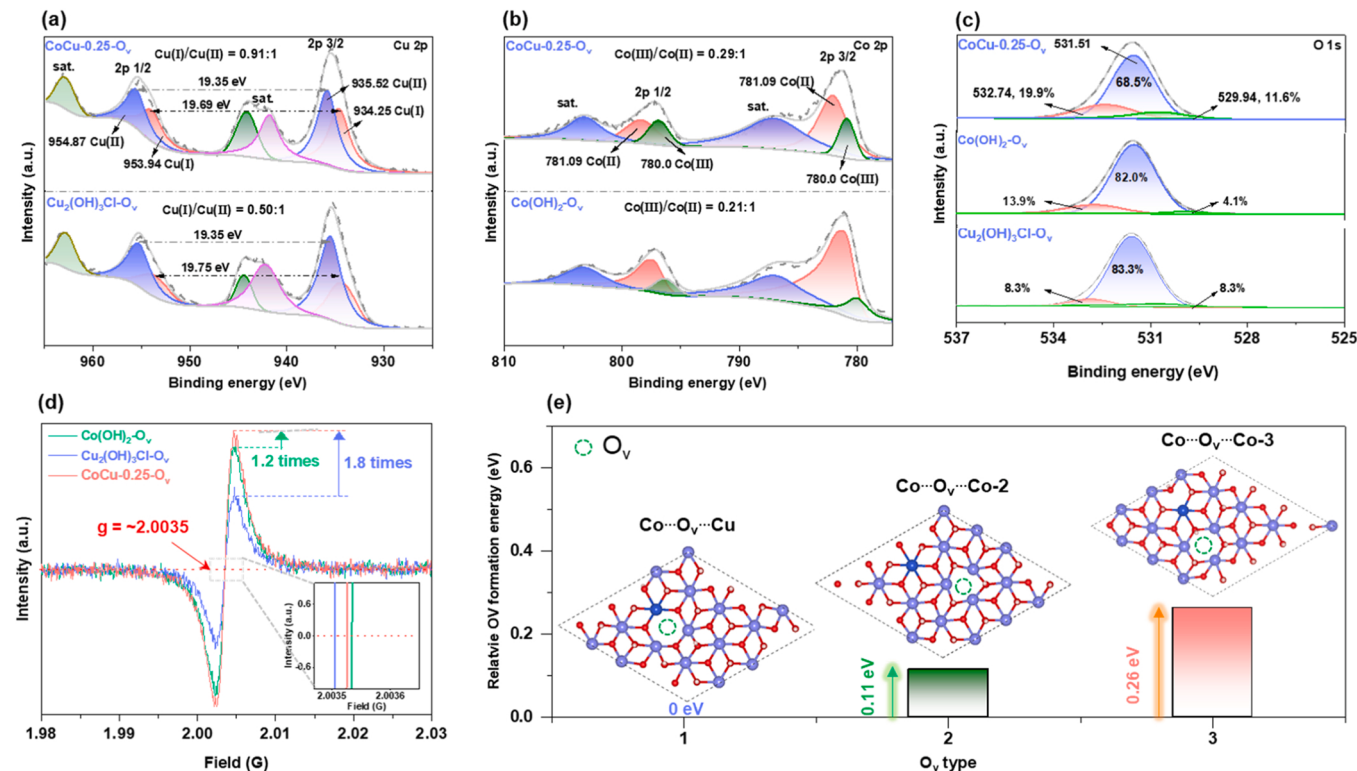


Fig. 2. Chemical structure of CoCu-0.25-O_v and two control materials: (a) Cu 2p XPS spectra, (b) Co 2p XPS spectra, (c) O 1s XPS spectra, (d) low-temperature (77 K) solid-state ESR spectra, and (e) relative formation energy of different O_v types.

samples are abundant with structural -OH groups. Generally, higher binding energy implies a decrease in average electron density of surface -OH group.[36] As shown in Fig. S6a, the binding energy of -OH of Cu₂(OH)₃Cl-O_v (in the form of Cu-OH-Cu) higher than that in Co(OH)₂-O_v (in the form of Co-OH-Co). This is due to the fact that Cu is more electronegative than Co, leading to the less electron density of -OH associated with Cu. Notably, the electron density of -OH in CoCu-0.25-O_v lies between the Co-OH-Co and Cu-OH-Cu. This suggests that the metal attached to the -OH ends of CoCu-0.25-O_v should be Co-OH-Cu, affirming the occurrence of interactive lattice substitution of Co and Cu. Note that the content of -OH in CoCu-0.25-O_v (68.5%) is much lower compared to the two control materials (82–83%), indicating that the loss of structural oxygen atom and newly created O_v in CoCu-0.25-O_v should be presented in the form of Co^{···}O_v^{···}Cu, where O_v is neighbored by both Co and Cu atoms with different properties (Fig. S5c). [16,37,38] The reduced peak intensity ratio of P₁(-OH)/P₂ (-OH) in CoCu-0.25-O_v in FT-IR (Fig. S6b) further corroborates the O_v is derived from the oxygen atom from -OH groups and exists in the form of Co^{···}O_v^{···}Cu in CoCu-0.25-O_v. In this case, O_v is the electron-rich site and the adjacent Co and Cu mainly act as two electron-poor regions, which is different the single electron-poor site generally reported in the previous works [16,22,39,40]. Also, the catalyst endowed with ternary reaction sites holds the high potential to exhibit higher catalytic activity compared to the controls with only one electron-rich (O_v) and one electron-poor (Cu or Co) sites.

The low-temperature (77 K) solid ESR spectra in Fig. 2d showcase obvious asymmetric peaks at the g value of ~2.0035 in these three samples, which are attributed to the unpaired single electrons trapped in the O_v.[8,29] Similar to the results of the O 1s XPS spectra, the O_v content of CoCu-0.25-O_v is the highest among the three samples, verifying the newly formed O_v in CoCu-0.25-O_v. O_v signal of Co^{···}O_v^{···}Cu in Co(OH)₂-O_v is more obvious than that of Cu^{···}O_v^{···} in Cu₂(OH)₃Cl-O_v, which might imply the O_v forms more readily on Co(OH)₂-O_v substrate. This could be because Co is less electronegative than Cu, resulting in oxygen

atoms coordinated with Co escaping more easily. Moreover, the g value position of CoCu-0.25-O_v also locates between Co(OH)₂-O_v and Cu₂(OH)₃Cl-O_v (inset in Fig. 2d bottom). This confirms that the newly generated O_v in CoCu-0.25-O_v should exist in the form of Co^{···}O_v^{···}Cu rather than Co^{···}O_v and Cu^{···}O_v.[16] In accordance with the trend in O 1s XPS spectra (Fig. S6a), the g value location of CoCu-0.25-O_v is much closer to that of Co(OH)₂-O_v, which clarifies that Co^{···}O_v^{···}Cu structure is more inclined to be introduced into the substrate of Co(OH)₂-O_v through interactive lattice substitution.[16].

Further, the formation energy of different types of O_v on CoCu-0.25-O_v is calculated and displayed in Fig. 2e. Co^{···}O_v^{···}Cu presents 0.11 eV and 0.26 eV lower O_v formation energy than that of Co^{···}O_v^{···}Co-2 and Co^{···}O_v^{···}Co-3, respectively, manifesting that asymmetric Co^{···}O_v^{···}Cu formed on CoCu-0.25-O_v is indeed energetically preferred.

3.3. Enhanced removal performance and PMS utilization rate over CoCu-0.25-O_v

The catalytic activities of the prepared samples are evaluated through the degradation of DMA in the presence of PMS under unadjusted conditions. Surprisingly, CoCu-0.25-O_v exhibits extraordinary catalytic activity and PMS utilization efficiency compared to the individual Co(OH)₂-O_v and Cu₂(OH)₃Cl-O_v. For the catalytic activity, negligible DMA is removed in the presence of a solo catalyst or PMS (Fig. S7a). In the co-presence of CoCu-0.25-O_v and PMS, DMA is quickly eliminated with a degradation efficiency of 100% within 30 min (Fig. 3a). However, only 10% and 56% of DMA are abated within 30 min under identical reaction conditions in the Co(OH)₂-O_v/PMS and Cu₂(OH)₃Cl-O_v/PMS systems, respectively. Based on DMA removal kinetics fitted by a *Pseudo-first* order reaction, DMA abatement performance in the CoCu-0.25-O_v/PMS system (0.22 min⁻¹) is 28 folds and 16 folds higher than that of Co(OH)₂-O_v/PMS (0.008 min⁻¹) and Cu₂(OH)₃Cl-O_v/PMS (0.014 min⁻¹) systems, respectively (Fig. 3b). On the other hand, for the PMS consumption, its decomposition is

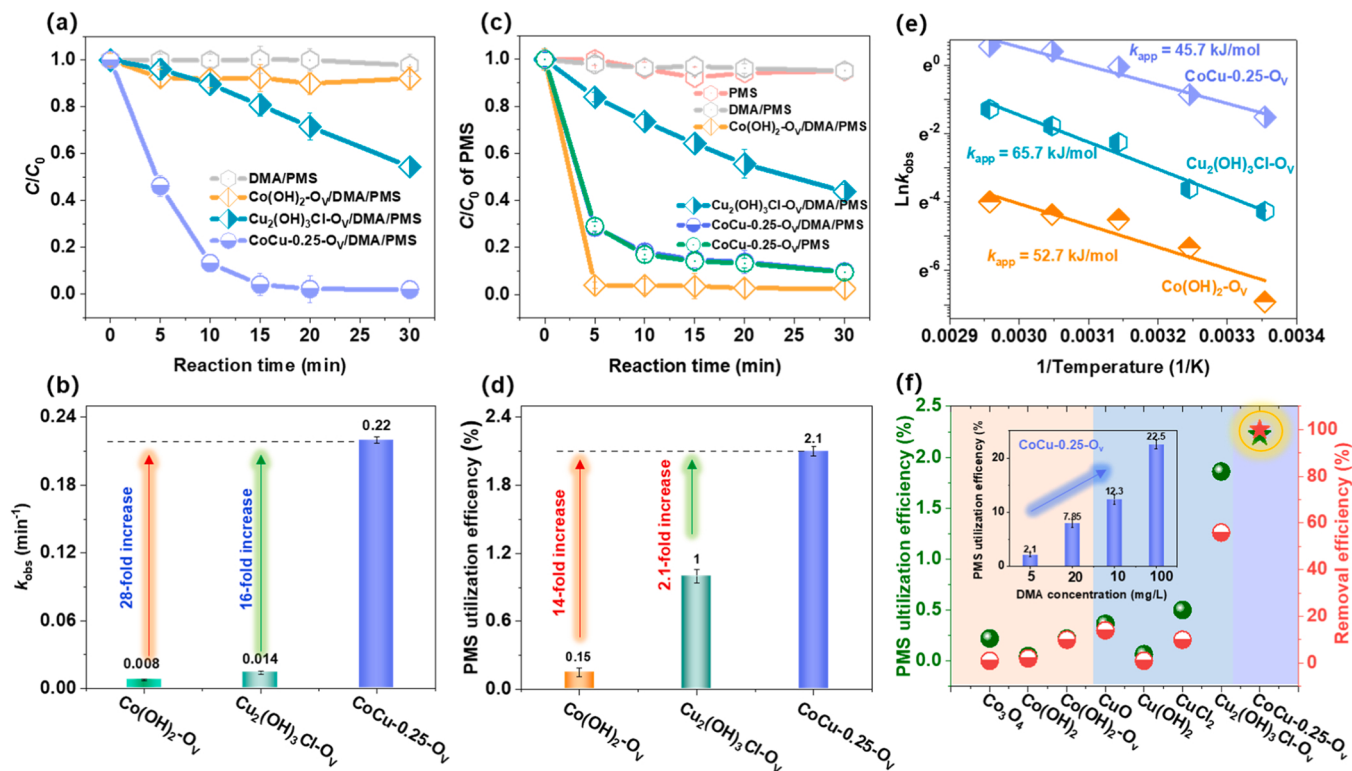


Fig. 3. (a) DMA degradation curves. (b) Reaction rate constant (k_{obs}). (c) PMS decomposition curves. (d) PMS utilization efficiency in different systems. (e) Arrhenius plots for DMA degradation over three catalysts. (f) Comparison of the PMS utilization rate and removal efficiency of DMA on CoCu-0.25-O_v and other Fenton-like catalysts (Inset: PMS utilization efficiency varying with DMA concentration). (Experimental conditions: [DMA] = 5 mg/L, [cat.] = 0.6 g/L, [PMS] = 5.88 mM).

unexpectedly not positively correlated with the DMA degradation. Around 91% of PMS is consumed within 30 min in the $\text{CoCu-0.25-O}_v/\text{PMS}$ system along with the fastest degradation of pollutant (Fig. 3c). On the contrary, PMS presents the fastest depletion with 100% decomposition before 5 min in the $\text{Co(OH}_2\text{-O}_v/\text{PMS}$ system, but accompanied by the lowest catalytic activity. Similar phenomenon is also found in the $\text{Cu}_2(\text{OH})_3\text{Cl-O}_v/\text{PMS}$ system, where around 60% of PMS is depleted while a moderate amount of DMA is oxidized during the same period. These findings illustrate that the PMS decomposition is not the only driving force for the efficient DMA degradation in $\text{CoCu-0.25-O}_v/\text{PMS}$ system. According to the amount of DMA degradation and PMS consumption, the calculated PMS utilization efficiency in the $\text{CoCu-0.25-O}_v/\text{PMS}$ ($\gamma = 2.1\%$) system is enhanced 14 folds and 2.1 folds relative to that of $\text{Co(OH}_2\text{-O}_v/\text{PMS}$ (0.15%) and $\text{Cu}_2(\text{OH})_3\text{Cl-O}_v/\text{PMS}$ (1%) systems, respectively (Fig. 3d, another calculation method for PMS utilization efficiency and discussion can be found in Fig. S7c of the supporting information). Note that both the removal performance and PMS utilization efficiency of DMA achieved on CoCu-0.25-O_v greatly surpass other the commercial catalysts including Co_3O_4 , Co(OH_2 , CuO , Cu(OH_2 and CuCl_2 under the identical environments (Fig. 3f), indicating that it has great application potential. Importantly, increasing the concentration of DMA from 5 to 100 mg/L can further effectively improve the utilization rate of PMS, with a maximum utilization rate of up to 22.5% in the $\text{CoCu-0.25-O}_v/\text{PMS}$ system (Inset Fig. 3f).

Based on above discussions, the excellent improvements in DMA removal and PMS utilization rate could originate from the formed asymmetric $\text{Co}^{\cdot\cdot}\text{O}_v\text{-Cu}$ sites on CoCu-0.25-O_v . To verify it, we analyzed the sources of activity of control materials with symmetric O_v , which was coordinated by the same metal atoms. For $\text{Co(OH}_2\text{-O}_v$, we found that DMA degradation rate (10%) is higher than that of commercial Co(OH_2 (2%) with less O_v content (Fig. S8). Meanwhile, PMS activation properties exhibit an improved trend over $\text{Co(OH}_2\text{-O}_v$ (ca. 90%)

compared to Co(OH_2 (ca. 80%) (Fig. 4b). These suggest that the presence of rich $\text{Co}^{\cdot\cdot}\text{O}_v$ of $\text{Co(OH}_2\text{-O}_v$ is responsible for 10% degradation of DMA and superior activation performance of PMS. Differently, these results clarify that a high-efficiency activation of PMS does not always lead to superior removal performance of DMA. This may be because the free DMA ($\text{pKa} = 10.7$) was present at the protonated state DMAH^+ at $\text{pH} \approx 3.5$ in the bulk phase (Fig. S7b), which is more significantly inert (11.59 eV for LUMO-HOMO energy gap) than the neutral one (7.59 eV for LUMO-HOMO energy gap) (Fig. S9). Similarly, neither commercial CuO , Cu(OH_2 , nor CuCl_2 can effectively degrade DMA in Fenton-like systems (Fig. 4c), although they present comparable PMS activation properties like $\text{Cu}_2(\text{OH})_3\text{Cl-O}_v$ (Fig. 4d). These prove that binary $\text{Cu}^{\cdot\cdot}\text{O}_v$ of $\text{Cu}_2(\text{OH})_3\text{Cl-O}_v$ is the main active site for 56% of DMA degradation. Note that the addition of DMA to $\text{Cu}_2(\text{OH})_3\text{Cl-O}_v/\text{PMS}$ system inhibits the decomposition of PMS, accompanied by a higher DMA removal, while the presence of DMA promotes PMS decomposition in $\text{Co(OH}_2\text{-O}_v/\text{PMS}$ system. These reveal DMA has a relatively strong interaction with $\text{Cu}^{\cdot\cdot}\text{O}_v$ site rather than $\text{Co}^{\cdot\cdot}\text{O}_v$ site and the former situation enables the restrained DMA at the catalyst surface to be consumed as an electron donor, i.e., DMA self-oxidation. In this case, DMA, as an electron donor, not only increases its removal, but also reduces PMS consumption by replacing PMS as an electron donor. Meanwhile, the activated DMA on the $\text{Cu}^{\cdot\cdot}\text{O}_v$ site is more vulnerable to ROS attacks for enhanced removal. This result was further verified by that less ROS is produced in $\text{Cu}_2(\text{OH})_3\text{Cl-O}_v/\text{PMS}$ system (Fig. 5d-f), but its efficiency in removing DMA exceeds that of $\text{Co(OH}_2\text{-O}_v/\text{PMS}$ system that produces more ROS. From the perspective of PMS and DMA activation, binary $\text{Cu}^{\cdot\cdot}\text{O}_v$ and $\text{Cu}^{\cdot}\text{O}_v$ are the most effective active sites to activate PMS and DMA, respectively. Accordingly, the fabrication of ternary $\text{Co}^{\cdot\cdot}\text{O}_v\text{-Cu}$ sites in CoCu-0.25-O_v is capable of realizing PMS and DMA co-activation at the same time. In addition, $\text{Co}^{\cdot\cdot}\text{O}_v\text{-Cu}$ sites make the confined DMA closer to the generated ROSs produced at active sites, which renders the

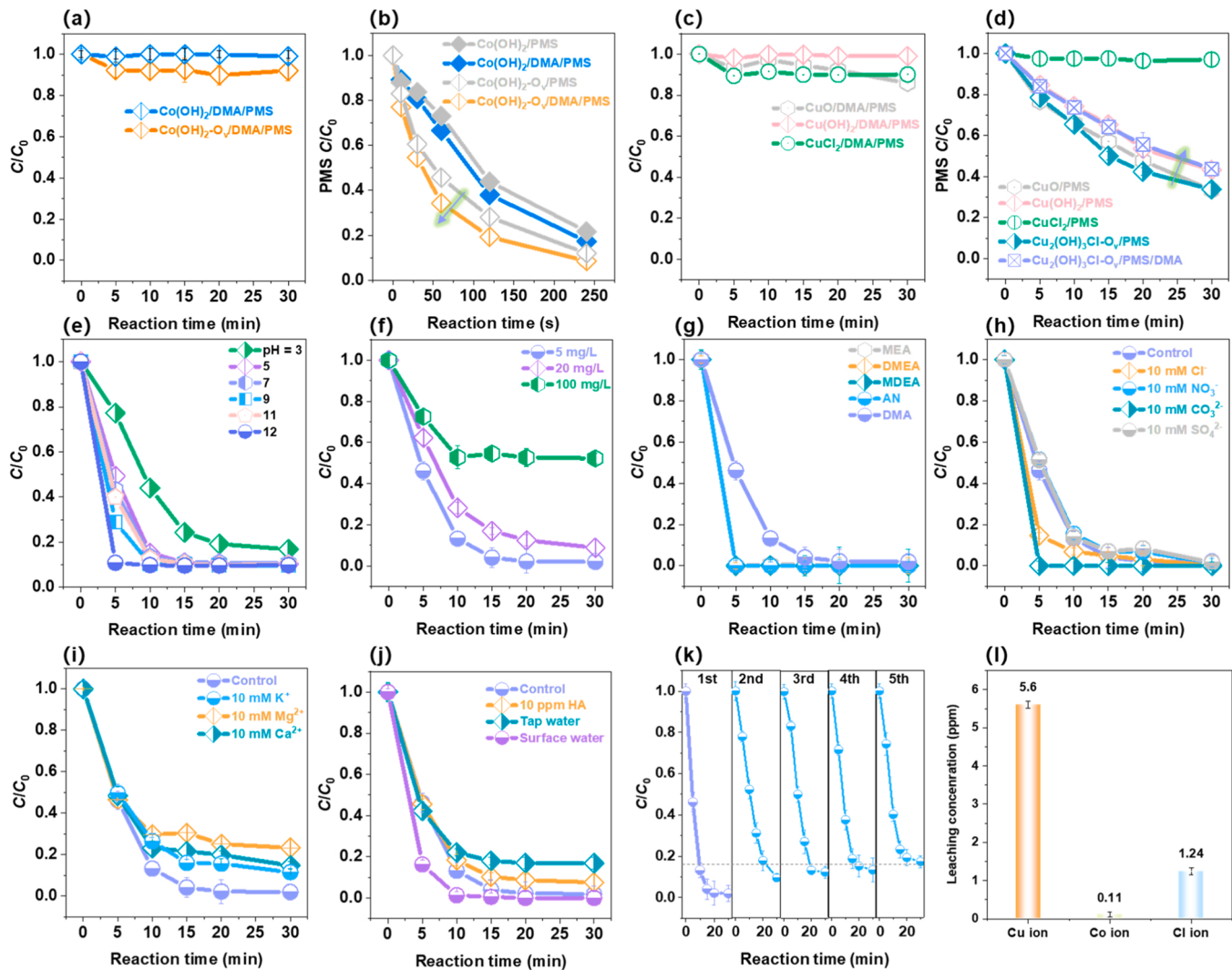


Fig. 4. (a) DMA degradation curves over $\text{Co(OH)}_2\text{-O}_v$ and commercial Co(OH)_2 . (b) PMS consumption over $\text{Co(OH)}_2\text{-O}_v$ and commercial Co(OH)_2 . (c) DMA degradation curves over commercial CuO , Cu(OH)_2 and CuCl_2 . (d) PMS consumption over $\text{Cu}_2(\text{OH})_3\text{Cl-O}_v$ and commercial CuO , Cu(OH)_2 and CuCl_2 . (e) Effect of initial pH values. (f) Effect of initial DMA concentration. (g) Effect of anions: Cl^- , HCO_3^- and CO_3^{2-} . (h) Effect of cations: K^+ , Ca^{2+} and Mg^{2+} . (i) Effects of HA and different water matrix on DMA degradation curves. (j) Different amines degradation over CoCu-0.25-O_v . (k) Recycle experiments using CoCu-0.25-O_v catalyst. (l) The leaching concentrations of Cu, Co and Cl ions during the CoCu-0.25-O_v reaction. (Experimental conditions: [DMA] = 5 mg/L, [cat.] = 0.6 g/L, [PMS] = 5.88 mM).

CoCu-0.25-O_v further achieve the significant improvement in DMA removal and PMS utilization efficiency due to the significantly shortened migration distance of ROSs.^[41]

In line with the above results, the apparent activation energies (E_a) obtained from kinetic experiments under different temperatures also show the same trend. As shown in Fig. 3e and Fig. S10, according to the Arrhenius equation, the calculated E_a of the $\text{CoCu-0.25-O}_v/\text{PMS}$ system (45.7 kJ/mol), is notably lower than that of $\text{Co(OH)}_2\text{-O}_v/\text{PMS}$ (52.7 kJ/mol) and $\text{Cu}_2(\text{OH})_3\text{Cl-O}_v/\text{PMS}$ (65.7 kJ/mol) systems. This demonstrates that asymmetric $\text{Co}^{\text{III}}\text{O}_v\text{-Cu}$ sites can considerably boost DMA oxidation by lowering E_a .

Additionally, the removal efficiency of total organic carbon (TOC) can reach as high as ~80% within 30 min in the $\text{CoCu-0.25-O}_v/\text{PMS}$ system (Fig. 5c). The excellent mineralization rate is the key to effectively inhibiting volatilization and reducing the environmental risk of intermediates as well as decreasing the post-treatment cost.^[42,43] TOC after 20 min keeps almost unchanged when the electron donor (DMA) is consumed completely during this period. This should be because strongly polar intermediates (more details can be found in production identification) released from the interface to the bulk phase, beyond the

“action zone”^[44] of short-lived ROS generated at the interface, preventing further mineralization.

Subsequently, the effect of the initial pH on the activity of CoCu-0.25-O_v is investigated (Fig. 4e). Unusually, in a wide pH range of 3 – 12, the catalyst shows strong activity for pollutant degradation. Even under extreme environments (pH = 3 and 12), the removal of DMA still reaches over 90% within 30 min. This finding demonstrates that CoCu-0.25-O_v has a wide working pH range, and its activity is not obviously affected by the acid–base environment. In general, the activity of metal catalysts is very sensitive to changes in pH because of the formation of surface hydroxyl groups at the metal sites (M–OH) in aqueous solution.^[16,45,46] However, CoCu-0.25-O_v avoids the pH effect on the activity, which could be largely attributed to the formation of O_v -mediated polarized surface that dominates the reaction process. Fig. 4f shows that DMA concentrations ranging from 5 to 20 mg/L of can achieve more than 90% removal efficiency, indicating this technology can meet different needs of different concentrations. However, when increasing the DMA concentration to 100 mg/L, only 50% of DMA can be oxidized, which could be attributed to limited active sites and less amount of ROSs relative to pollutants. As shown in Fig. 4g, all the

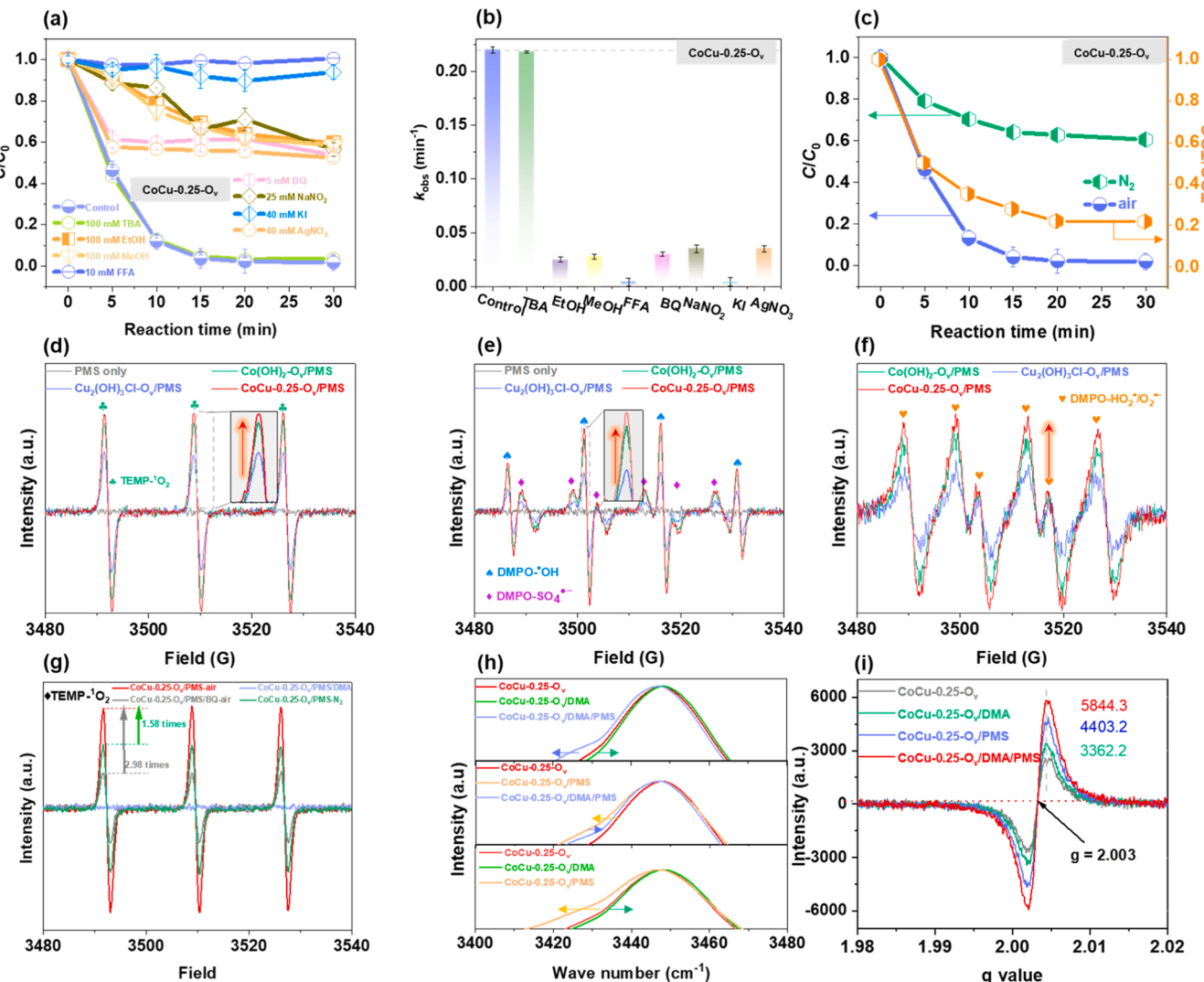


Fig. 5. (a) DMA degradation curves and (b) k_{obs} in the presence of different quenchers. (c) DMA degradation in the N_2 and air (normal) conditions (Experimental conditions: [DMA] = 5 mg/L, [cat.] = 0.6 g/L, [PMS] = 5.88 mM). ESR spectra of three samples obtained by spin trapping with (d) TEMP and (e, f) DMPO. (g) ESR spectra of $^1\text{O}_2$ in the presence of BQ and aerating N_2 for 30 min in advance in CoCu-0.25-O_v catalytic systems. (h) *In-situ* FT-IR peaks of CoCu-0.25-O_v in the presence of DMA and/or PMS. (i) *In-situ* solid ESR spectra of CoCu-0.25-O_v after reaction in different suspensions ([cat.] = 6 g/L, [PMS] = 58.8 mM, [DMA] = 50 ppm, [DMPO] = [TEMP] = 100 mM).

selected amines with different structures (Fig. S11) can be 100% removed within 5 min, even showing better removal performance than DMA. This is assigned to the fact that DMA is the secondary or terminal oxidation product of these amines, which makes it feature with a stronger antioxidant capacity.

To investigate the universal applicability of the catalyst, the influences of various anions, cations natural organic matter (NOM) and different water matrixes on DMA removal were considered. As shown in Fig. 4h, even 10 mM of NO_3^- and SO_4^{2-} show no influence on DMA removal. Co-existence of Cl^- and CO_3^{2-} promotes the DMA degradation. The reason for the former may be that excessive Cl^- can react with $\text{HSO}_5^-/\text{SO}_4^{2-}$ to produce reactive chlorine species (HClO , Cl^\bullet , Cl_2^\bullet , and ClO^\bullet), which are selective radicals and prefer to react with electron-rich moieties of DMA. [47] The latter increment is due to the fact that CO_3^{2-} possessing a buffering ability can maintain a more basic pH of the reaction system than the control after the addition of PMS, thus promoting the removal of DMA. This is in agreement with DMA removal efficiency increasing as pH rises (Fig. 4e). By contrast, the presence of coexisting cations (Ca^{2+} , K^+ , and Mg^{2+}) inhibited about 20% of DMA removal. The electrostatic interaction forces could make high concentrations of

cations (10 mM cations vs 5.88 mM PMS) tend to combine with negatively charged PMS, thus preventing partial PMS from approaching the catalyst interface. Fig. 4i describes that the presence of humic acid (HA), a representative NOM, with a concentration of 10 mg/L, had a slight inhibition effect on DMA degradation, indicating a good resistance to NOM. Fig. 4j illustrates that DMA displays more than 88% of removal both in the tap water and surface water, while the tap water and surface water tend to have opposite effects on DMA removal. This might be the fact that tap water could contain more cations, while surface water includes more Cl^- and/or CO_3^{2-} .

Afterward, we evaluate the stability and durability of the CoCu-0.25-O_v structure by recycling experiments, measuring the leaching of Co, Cu, and Cl in the solution, and re-characterizing the used samples through XRD, XPS, and FT-IR. As shown in Fig. 4k, 85% of DMA degradation was still achieved after the fifth run. ICP-OES measurement proved that small amounts of Co (0.11 ppm), Cu (5.6 ppm), and Cl (1.24 ppm) ions leached into the solution after the reaction under the optimal conditions. Among them, the leaching concentration of relatively more toxic Co is lower than the stringent limit of 1 mg/L for the manufacturing effluents of the Taiwan industry. Homogeneous experiments are carried out with

Co, Cu, and Cl ions under the same conditions (Fig. S12). Results show that the target is oxidized less than 8% in both $\text{Co}^{2+}/\text{Cl}^-/\text{PMS}$ and $\text{Cu}^{2+}/\text{Cl}^-/\text{PMS}$ systems, indicating that the pollutant removal predominantly originates from the heterogeneous catalyst. Further, the main peaks in the XRD, XPS, and FT-IR (Fig. S13-15) remain before and after the reaction without obvious shift and change, implying the satisfactory stability of the underlying structure of $\text{CoCu-0.25-O}_\text{v}$.

3.4. Origin of enhanced catalytic activity and PMS utilization efficiency

To further elucidate the mechanism of dual improvements in catalytic activity and PMS utilization efficiency over $\text{CoCu-0.25-O}_\text{v}$ catalyst, radical quenching experiments and ESR characterizations were conducted. As shown in Fig. 5a, b, after adding $\cdot\text{OH}$ scavenger ($k_{\cdot\text{OH}/\text{TBA}} = 3.8-7.6 \times 10^8 \text{ M}^{-1}\text{s}^{-1}$) [48], tert butyl alcohol (TBA), into the reaction system, no significant inhibition of activity was observed. This indicates that the $\cdot\text{OH}$ in the bulk solution was not able to attack protonated DMA with low reactivity when pH of system is below 4.5 (Fig. S7b), far from its pK_a (10.7) [48]. The introduction of ethanol (EtOH), as SO_4^{2-} and $\cdot\text{OH}$ quencher, ($k_{\text{SO}_4^{2-}/\text{EtOH}} = (1.6-7.7) \times 10^7 \text{ M}^{-1}\text{s}^{-1}$, $k_{(\cdot\text{OH}, \text{EtOH})} = (1.2-2.8) \times 10^9 \text{ M}^{-1}\text{s}^{-1}$) inhibits about 50% of DMA degradation. Further, after adding furfuryl alcohol (FFA) (${}^1\text{O}_2$ trapping agent, $k_{\text{O}_2/\text{FFA}} = 1.2 \times 10^8 \text{ M}^{-1}\text{s}^{-1}$) [48], no degradation activity of DMA was observed. These results collectively suggest that ${}^1\text{O}_2$ plays the primary role in the DMA degradation, followed by the SO_4^{2-} radicals. Besides, the electron transfer pathway that DMA was oxidized by the formed PMS^* on the catalyst surface was eliminated by the amperometry *i-t* curves in the $\text{CoCu-0.25-O}_\text{v}/\text{PMS}$ system (Fig. S16a, the detailed discussion can be found in the supporting information) [49]. Furthermore, ESR measurements were carried out to directly substantiate ROSSs among the different systems. DMPO and TEMP were selected as trapping agents for SO_4^{2-} , $\cdot\text{OH}$, O_2^- and ${}^1\text{O}_2$, respectively. By using TEMP as a trapping agent ($k_{\text{O}_2/\text{TEMP}} = 5.3 \times 10^5 \text{ M}^{-1}\text{s}^{-1}$), the strong characteristic signals in Fig. 5d, were attributed to TEMP- ${}^1\text{O}_2$, verifying the generation of ${}^1\text{O}_2$. Add the stronger characteristic signal observed in the $\text{CoCu-0.25-O}_\text{v}/\text{PMS}$ system under equal conditions shows that the amount of ${}^1\text{O}_2$ is much more than the two controls. This demonstrates that $\text{CoCu-0.25-O}_\text{v}$ containing ternary $\text{Co}^{\cdot\cdot\cdot}\text{O}_\text{v}\cdot\text{Cu}$ site is a more effective for ${}^1\text{O}_2$ production than two catalysts with binary $\text{Co}^{\cdot\cdot\cdot}\text{O}_\text{v}$ and $\text{Cu}^{\cdot\cdot\cdot}\text{O}_\text{v}$ sites. Similarly, the strongest DMPO- SO_4^{2-} , DMPO- $\cdot\text{OH}$ (Fig. 5e) and DMPO- $\text{HO}_2^-/\text{O}_2^-$ (Fig. 5f) ESR signal were also observed in $\text{CoCu-0.25-O}_\text{v}/\text{PMS}$ system among three systems, suggesting that ternary $\text{Co}^{\cdot\cdot\cdot}\text{O}_\text{v}\cdot\text{Cu}$ sites can also promote the radical's generation relative to the binary ones. Note that the evident $\cdot\text{OH}$ signal in ESR is assigned to the fast transformation of DMPO- SO_4^{2-} to DMPO- $\cdot\text{OH}$ after reaction with H_2O [7].

Since ${}^1\text{O}_2$ is the main active species, we further explored the specific source. It has been reported that ${}^1\text{O}_2$ mainly comes from the DO activation and PMS activation, in which PMS acts as an electron donor (Pathway I) in the O_v -rich catalyst or generated O_2^- by PMS decomposition [29,50]. First, for identifying the pathway of DO activation, we carried out DMA degradation experiment in $\text{CoCu-0.25-O}_\text{v}$ Fenton-like system under the nitrogen (N_2) atmosphere. As shown in Fig. 5c, it is surprised to find that after DO in reaction solution discharged by bubbling N_2 in advance for 30 min, DMA degradation efficiency drops sharply from 100% to $\sim 40\%$. This finding reveals that DO activation contributed about 60% to the degradation of DMA. This result highly demonstrated the efficient utilization of endogenous compounds. On the other hand, O_2^- was observed in the $\text{CoCu-0.25-O}_\text{v}$ system via ESR characterization (Fig. 5f), which was further verified by that p-benzoquinone (BQ, a quencher for O_2^-) can also suppress around 60% of DMA degradation (Fig. 5a, b). The above almost the same suppression trends prove that O_2^- are mainly from the DO activation, rather than the decomposition of PMS. The addition of AgNO_3 , as an electron quencher, makes the removal efficiency of DMA decrease by $\sim 40\%$, verifying the presence of electron transfers from the O_v to O_2 for O_2^- generation.

Therefore, combined with the above three aspects of experimental results and literature reports, [29,50,51] DO over $\text{CoCu-0.25-O}_\text{v}$ serves as an electron acceptor receiving one electron from electron-rich O_v to generate O_2^- and subsequently disproportionate to form ${}^1\text{O}_2$. Further, semi-quantification results of ESR display that in the presence of BQ, the concentration of ${}^1\text{O}_2$ ($1.5 \times 10^{-5} \text{ M}$) production decreased by about three-fourths compared to that system without BQ addition ($4.5 \times 10^{-5} \text{ M}$) (Fig. S16b). This verifies that around three-fourths of ${}^1\text{O}_2$ species are primarily generated from DO activation. In this case, the remaining one-fourth of ${}^1\text{O}_2$ mainly derives from the oxidation of PMS, which undergoes terminal O-H breakage to generate ${}^1\text{O}_2$ through the recombination of two SO_5^- intermediates (Pathway I) [9,10]. The introduction of NaNO_2 (a quencher for SO_5^-) [52], is capable of preventing DMA degradation by $\sim 50\%$, affirming that the existence of SO_5^- . It is noted that with the addition of DMA into the $\text{CoCu-0.25-O}_\text{v}/\text{PMS}$ system, no TEMP- ${}^1\text{O}_2$ signal was observed. This indicates that the ${}^1\text{O}_2$ generated at the $\text{Co}^{\cdot\cdot\cdot}\text{O}_\text{v}\cdot\text{Cu}$ site is immediately consumed by the DMA confined at the same sites, confirming that DMA interacting with the interface is very close to ${}^1\text{O}_2$. As a result, the TEMP cannot capture the ${}^1\text{O}_2$ signal in the bulk phase [53]. To further affirm ROS generated and functioned at the interface, we introduced KI as a scavenger for all the surface radicals. The result illustrated that KI inhibited almost 100% of DMA degradation, which verified all the related active species or intermediates (O_2^- , SO_5^- and SO_4^{2-}) indeed come from the catalyst interface. In other words, these interfacial ROSSs are easier to access the DMA at the near site due to the shortened migration distance of ROSSs [41], and thus achieving excellent abatement performance.

Based on these, we can conclude that DMA degradation was mainly attributed to the interfacial ${}^1\text{O}_2$, followed by the SO_4^{2-} radical. For the dominant ${}^1\text{O}_2$, around three-fourths of which is chiefly derived from DO activation, in which O_2 molecules undergo one-electron-reduction for O_2^- production and subsequently disproportionate to form ${}^1\text{O}_2$, and the residual one-fourth of ${}^1\text{O}_2$ originates from the recombination of SO_5^- from PMS oxidation.

Given the simultaneous existence of DO, DMA, and PMS in the system, *in-situ* FT-IR and *in-situ* ESR experiments are performed to investigate the role of electron acceptor and donor in the reaction system. As displayed in Fig. 5h, compared with bare $\text{CoCu-0.25-O}_\text{v}$, the FT-IR peak of $\text{CoCu-0.25-O}_\text{v}/\text{DMA}$ slightly shifts to high wavenumbers, indicating DMA as the electron donor donates electrons to the catalyst surface leading to the enhancement of electron density. After further addition of PMS, the peak shifts slightly to lower wavenumbers, indicating PMS mainly acts as an electron acceptor (Pathway II), which is further verified by the result of $\text{CoCu-0.25-O}_\text{v}/\text{PMS}$ compared to $\text{CoCu-0.25-O}_\text{v}$. This is consistent with that only one-fourth of ${}^1\text{O}_2$ comes from PMS acting as an electron donor and most PMS as electron acceptor undergoes O-O bond breaking for releasing SO_4^{2-} . Notably, the utilization rate of PMS can be improved when PMS is as an electron acceptor compared to the PMS as an electron donor. This is because two PMS molecules are required to produce only one ROS of ${}^1\text{O}_2$ (Pathway I), while only one PMS is needed to form one SO_4^{2-} (Pathway II) [9,10]. Furthermore, *in-situ* ESR signal of single electron on the $\text{CoCu-0.25-O}_\text{v}$ exhibits an increasing trend when co-exists with DMA or PMS compared to the individual catalyst (Fig. 5i). This indicates that $\text{CoCu-0.25-O}_\text{v}$ surface is in an extremely electron-deficient state due to the formation of abundant O_v after interactive lattice substitution of Co-Cu sites, thus easily snatching electrons from surroundings [16]. The ESR signal of single electron on the $\text{CoCu-0.25-O}_\text{v}$ further improves to the highest (intensity: 5844) when co-exists with DMA and PMS at the same time. The signal is higher than the combined signal intensity (intensity: 5402) of $\text{DAM/CoCu-0.25-O}_\text{v}$ and $\text{PMS/CoCu-0.25-O}_\text{v}$ alone. This suggests that more or stronger electron acceptors should exist in the $\text{CoCu-0.25-O}_\text{v}/\text{DMA}/\text{PMS}$ system. Combined with the above discussion, the stronger electron acceptor should be O_2 , which contributes largely to DMA degradation in the reaction system.

Overall, the newly formed ternary $\text{Co}^{\cdot\cdot\cdot}\text{O}_\text{v}\cdot\text{Cu}$ sites in $\text{CoCu-0.25-O}_\text{v}$

trigger the co-activation of interfacial DMA and O_2 substituting PMS as electron donors and acceptors, respectively, accompanied by the enhancement of ROSs generation and shortening their migration distances to interfacial DMA, thus reducing PMS consumption and boosting DMA degradation.

To further unveil the role of $Co^{...}O_v^{...}Cu$ sites in $CoCu-0.25-O_v$ for the substantial enhancements of catalytic performance at the molecular level, DFT investigations were performed. The $Co^{...}O_v$ -containing $Co(OH)_2-O_v$ catalyst is constructed to simulate our $Co(OH)_2-O_v$. According to the experimental results, the $Co^{...}O_v^{...}Cu$ structure is introduced into the single-layer $Co(OH)_2-O_v$ substrate to represent our $CoCu-0.25-O_v$.

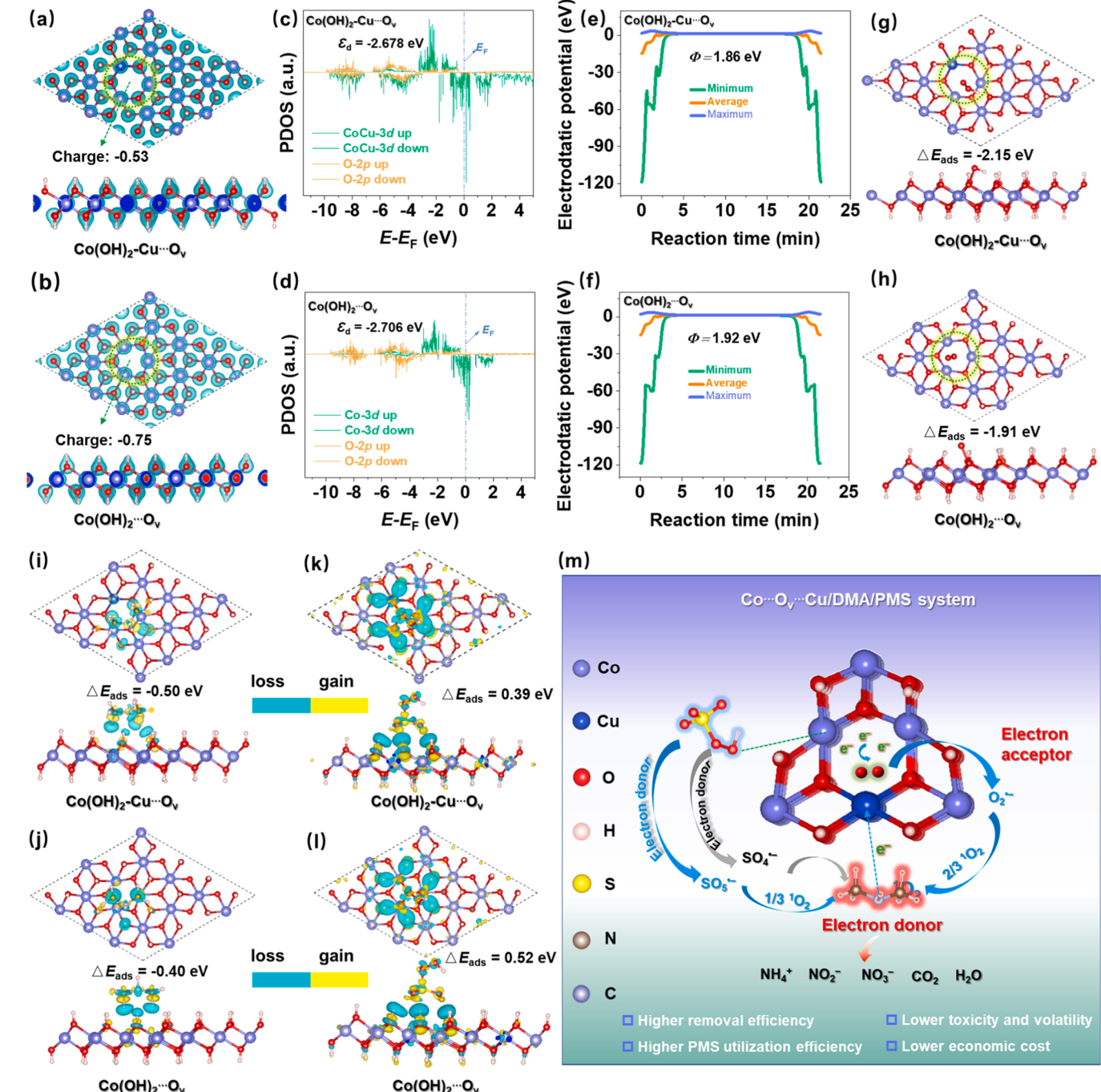


Fig. 6. (a-b) Optimized structures and electron density of both substrates. The marked yellow circle is the multifunctional microregion; (c-d) PDOS of metal 3d, and O_2p orbitals; (e-f) Work function analysis; (g-h) O_2 adsorption configurations on both substrates; Electron density difference of DMA (i-j) and PMS (k-l) after adsorption. The isosurface contour is 0.001 e/bohr, and the blue and yellow denote electron depletion and accumulation, respectively. (m) Schematic illustration of enhanced DMA degradation with higher PMS utilization rate via efficient utilization of endogenous electron donor/acceptor.

introduction of Cu (Fig. S5b-c). The electron deficiency of $\text{Co}^{\cdot\cdot}\text{O}_\text{v}\text{Cu}$ microarea also indicates that it is more likely to snatch electrons from peripheral DMA and thus activates DMA as an electron donor.[29] The projected density of states (PDOS) analysis shows that the *d*-band center of $\text{Co}(\text{OH})_2\text{-Cu}^{\cdot\cdot}\text{O}_\text{v}$ (−2.678 eV, Fig. 6c) is much closer to the Fermi level than that of $\text{Co}(\text{OH})_2\text{-O}_\text{v}$ (−2.706 eV, Fig. 6d), which is beneficial to the adsorption of reactants and following interfacial reactions.[33] Also, PDOS analysis highlights a more significant overlap between 3d of Co and Cu and O 2p in $\text{Co}(\text{OH})_2\text{-Cu}^{\cdot\cdot}\text{O}_\text{v}$ than that of Co 3d and O 2p in $\text{Co}(\text{OH})_2\text{-O}_\text{v}$. This illustrates the more orbital and electronic interactions of metal and O exist in $\text{Co}(\text{OH})_2\text{-Cu}^{\cdot\cdot}\text{O}_\text{v}$, which would contribute to improved catalytic activity.[7,54,55] Moreover, the lower work function is found in $\text{Co}(\text{OH})_2\text{-Cu}^{\cdot\cdot}\text{O}_\text{v}$ (1.86 eV, Fig. 6e) than that of $\text{Co}(\text{OH})_2\text{-O}_\text{v}$ (1.92 eV, Fig. 6f), indicating $\text{Co}(\text{OH})_2\text{-Cu}^{\cdot\cdot}\text{O}_\text{v}$ benefits more the following redox reactions of reactants on the catalyst surface.[56,57] Overall, the $\text{Co}^{\cdot\cdot}\text{O}_\text{v}\text{Cu}$ -containing $\text{Co}(\text{OH})_2\text{-Cu}^{\cdot\cdot}\text{O}_\text{v}$ would favor the adsorption and following activation of reactants at the catalyst interface.

Ulteriorly, the adsorptions of O_2 , DMA, and PMS on the catalyst surface were conducted to explore the interaction mechanism between three reactants and multifunctional microregion, and confirm the role of reactants as electron donor-acceptor from the microscopic perspective. As shown in Fig. 6 g-h, O_2 molecules are significantly trapped in the middle of O_v due to the imprinting effect[29,50] and both exhibit Pauling-type adsorption configuration.[58] It should be mentioned that the adsorbed O_2 can directly generate $^*\text{OOH}$ on the $\text{Co}(\text{OH})_2\text{-Cu}^{\cdot\cdot}\text{O}_\text{v}$ (Fig. 6g), instead of the common $^*\text{O}_2$ on the $\text{Co}(\text{OH})_2\text{-O}_\text{v}$ (Fig. 6h).[29] This indicates that O_2 molecule on the surface of $\text{Co}(\text{OH})_2\text{-Cu}^{\cdot\cdot}\text{O}_\text{v}$ catalyst has higher reactivity and thus can grab hydrogen from the neighboring -OH. This should be favored by the local electron non-equilibrium distribution around $\text{Co}^{\cdot\cdot}\text{O}_\text{v}\text{Cu}$ microenvironment.[58, 59] Correspondingly, the adsorption energy of O_2 on $\text{Co}(\text{OH})_2\text{-Cu}^{\cdot\cdot}\text{O}_\text{v}$ is lower than that of $\text{Co}(\text{OH})_2\text{-O}_\text{v}$ (−2.15 eV vs −1.91 eV), indicating the $\text{Co}^{\cdot\cdot}\text{O}_\text{v}\text{Cu}$ microarea is indeed preferential for O_2 adsorption and subsequent reaction[29]. The above results suggest that the $\text{Co}^{\cdot\cdot}\text{O}_\text{v}\text{Cu}$ of $\text{Co}(\text{OH})_2\text{-Cu}^{\cdot\cdot}\text{O}_\text{v}$ can strengthen the role of O_2 as an electron acceptor by virtue of relatively stronger adsorption and higher reactivity, and promoting synchronously the generation of O_2 -involved ROSSs including $\text{O}_2^{\cdot-}$ and $^1\text{O}_2$. This well explains the enhanced ESR signal of $\text{HO}_2^{\cdot}/\text{O}_2^{\cdot-}$ and $^1\text{O}_2$ found in Fig. 5d, f.

Unlike O_2 molecules, DMA and PMS exhibit relatively weaker electronic interactions with the surface of the catalyst in their adsorption configurations. As displayed in Fig. 6i-j, the adsorbed DMA molecules are both a little far from the catalyst surfaces, and their orientations are slightly different from each other. Since the N atom in DMA is more polar than -CH₃, the electron donor is mainly adsorbed on the catalyst surface through the interaction between N and metal ions. Therefore, as a potential reactive site, the N atom of DMA[60-62] has fewer valence electrons (6.06 e vs 6.23 e) on the $\text{Co}(\text{OH})_2\text{-Cu}^{\cdot\cdot}\text{O}_\text{v}$ surface relative to that of $\text{Co}(\text{OH})_2\text{-O}_\text{v}$. Also, the N-H (*l* = 1.0209 Å vs 1.0208 Å) and C-N (*l* = 1.463 Å vs 1.460 Å) bond lengths of DMA on the $\text{Co}(\text{OH})_2\text{-Cu}^{\cdot\cdot}\text{O}_\text{v}$ are relatively longer than those on $\text{Co}(\text{OH})_2\text{-O}_\text{v}$ surface.[28] These results indicate that DMA is preferential to acting as an electron donor on $\text{Co}(\text{OH})_2\text{-Cu}^{\cdot\cdot}\text{O}_\text{v}$ catalyst, and is activated more easily by breaking bonds to facilitate the subsequent reaction.[49] This result well explains the above findings that the addition of DMA into $\text{Co}(\text{OH})_2\text{-O}_\text{v}$ /PMS system accelerates PMS decomposition while not improves the PMS consumption in $\text{CoCu-0.25-O}_\text{v}$ /PMS system (Figs. 4b and 3c). This is because DMA in the formed system is free in the bulk phase while DMA is activated as electron donor at the catalyst interface in the latter system. As for the PMS molecules, they present similar adsorption configurations on the two catalyst surfaces (Fig. 6k-l). The adsorption energy of PMS on $\text{Co}(\text{OH})_2\text{-Cu}^{\cdot\cdot}\text{O}_\text{v}$ is relatively lower in comparison with $\text{Co}(\text{OH})_2\text{-O}_\text{v}$ (0.39 eV vs 0.52 eV), indicating the interaction between PMS and $\text{Co}(\text{OH})_2\text{-Cu}^{\cdot\cdot}\text{O}_\text{v}$ surface is relatively stronger. Electron density difference analysis evidence that more notable electronic interaction is found when PMS is adsorbed on the $\text{Co}(\text{OH})_2\text{-Cu}^{\cdot\cdot}\text{O}_\text{v}$ surface. Moreover, the whole

PMS adsorbed on the $\text{Co}(\text{OH})_2\text{-Cu}^{\cdot\cdot}\text{O}_\text{v}$ catalyst has a lower charge relative to that of $\text{Co}(\text{OH})_2\text{-O}_\text{v}$ (−0.945 vs −0.952), suggesting more electrons are transferred from the $\text{Co}(\text{OH})_2\text{-Cu}^{\cdot\cdot}\text{O}_\text{v}$ surface to PMS in the adsorption configuration, which is substantiated by the sharpest ΔI decrease observed after PMS was added to the $\text{CoCu-0.25-O}_\text{v}$ (Fig. S16a). [49,63] These results demonstrate that PMS, mainly as an electron acceptor, is more conducive to $\text{SO}_4^{\cdot-}$ generation through a single-electron-reduction, which well supports the reinforced $\text{SO}_4^{\cdot-}$ signal in ESR.

Based on the theoretical and experimental results, the mechanism for the enhancements of catalytic activity and PMS utilization efficiency is unveiled in Fig. 6 m. Compared to the controls, the construction of electron-polarized $\text{Co}^{\cdot\cdot}\text{O}_\text{v}\text{Cu}$ multifunctional sites on $\text{CoCu-0.25-O}_\text{v}$ triggers the co-adsorption and co-activation of DMA, O_2 molecules, and PMS on the catalytic interface by pushing the *d*-band center of the catalyst closer to the Fermi level and lowering the function work, is the key to realizing the substitution of electron donor and acceptor. Specifically, $\text{Co}^{\cdot\cdot}\text{O}_\text{v}\text{Cu}$ site can facilitate the activation and bond breaking of endogenous DMA, thus replacing partial PMS as an electron donor. On the other hand, the endogenous DO molecules can be activated more easily at the $\text{Co}^{\cdot\cdot}\text{O}_\text{v}\text{Cu}$ microenvironment and undergoes one-electron-reduction to form more $\text{O}_2^{\cdot-}$ followed by evolving into abundant $^1\text{O}_2$. This pathway contributes approximately three-fourths of $^1\text{O}_2$ in the reaction system, the only one-fourth comes from the reduction of PMS, thus reducing PMS consumption. Besides, $\text{Co}^{\cdot\cdot}\text{O}_\text{v}\text{Cu}$ site improves the reactivity of DO and enhances the electron-accepting ability of PMS, resulting in the production of more $^1\text{O}_2$ and $\text{SO}_4^{\cdot-}$. Consequently, the utilization of endogenous donor (DMA) and acceptor (DO) at the $\text{Co}^{\cdot\cdot}\text{O}_\text{v}\text{Cu}$ site leads to lower PMS consumption and enhanced ROSSs production. Meanwhile, the confined and activated DMA at the interface degrades more easily through self-oxidation and the attacking of the near-generated $^1\text{O}_2$ and $\text{SO}_4^{\cdot-}$ (Fig. S17) into products with lower toxicity and volatility (Details can be found in the following section). Thereby, dual remarkable increases in DMA abatement performance and PMS utilization efficiency were achieved at the $\text{Co}^{\cdot\cdot}\text{O}_\text{v}\text{Cu}$ sites.

3.5. Toxicity, volatility assessment and economic evaluations

IC and HPLC were collectively to identify the possible products. As shown in Fig. 7a, the intermediates mainly include and follow the order: $\text{NO}_2^- > \text{NO}_3^- > \text{NH}_4^+ > \text{HCOOH} > \text{CH}_3\text{COOH} > \text{MA}$. All the products especially the NO_2^- increased with the reaction time, indicating the rapid DMA transformation. DMA is hazardous to the atmosphere and water environment due to its strong volatility and potential toxicity.[3] Therefore, both the toxicity and volatility of its oxidation products need to be further evaluated. As shown in Fig. 7d-j, considering that NO_2^- can rapidly be oxidized into harmless NO_3^- under air conditions, the acute and chronic toxicities of intermediates to the fish, Daphnia, and green algae were considerably decreased compared with DMA. Their volatility of oxidation products is evaluated based on Henry's constant. As shown in Fig. 7b, all Henry's constants of intermediates were lower than DMA, implying decreased volatility. Thus, the degradation of DMA in the $\text{CoCu-0.25-O}_\text{v}$ /PMS system belonged to the process of toxicity and volatility reduction, further confirming the practical application potential of the eco-friendly catalytic system. To assess an economical comparison of technologies employed, the electric energy per order of pollutant removal (EE/O) was calculated (More details can be found in Text S3).[19,64] As shown in Fig. 7c, the EE/O value of the $\text{CoCu-0.25-O}_\text{v}$ /PMS system is 0.011 kWh/L, which is respectively about 44 and 6.2 times lower than that of the $\text{Co}(\text{OH})_2\text{-O}_\text{v}$ /PMS system (0.479 kWh/L) and $\text{Cu}_2(\text{OH})_3\text{Cl-O}_\text{v}$ /PMS system (0.068 kWh/L). The lower energy consumption is of great significance for practical applications.

4. Conclusions

We have successfully synthesized a composite catalyst $\text{CoCu-0.25-O}_\text{v}$

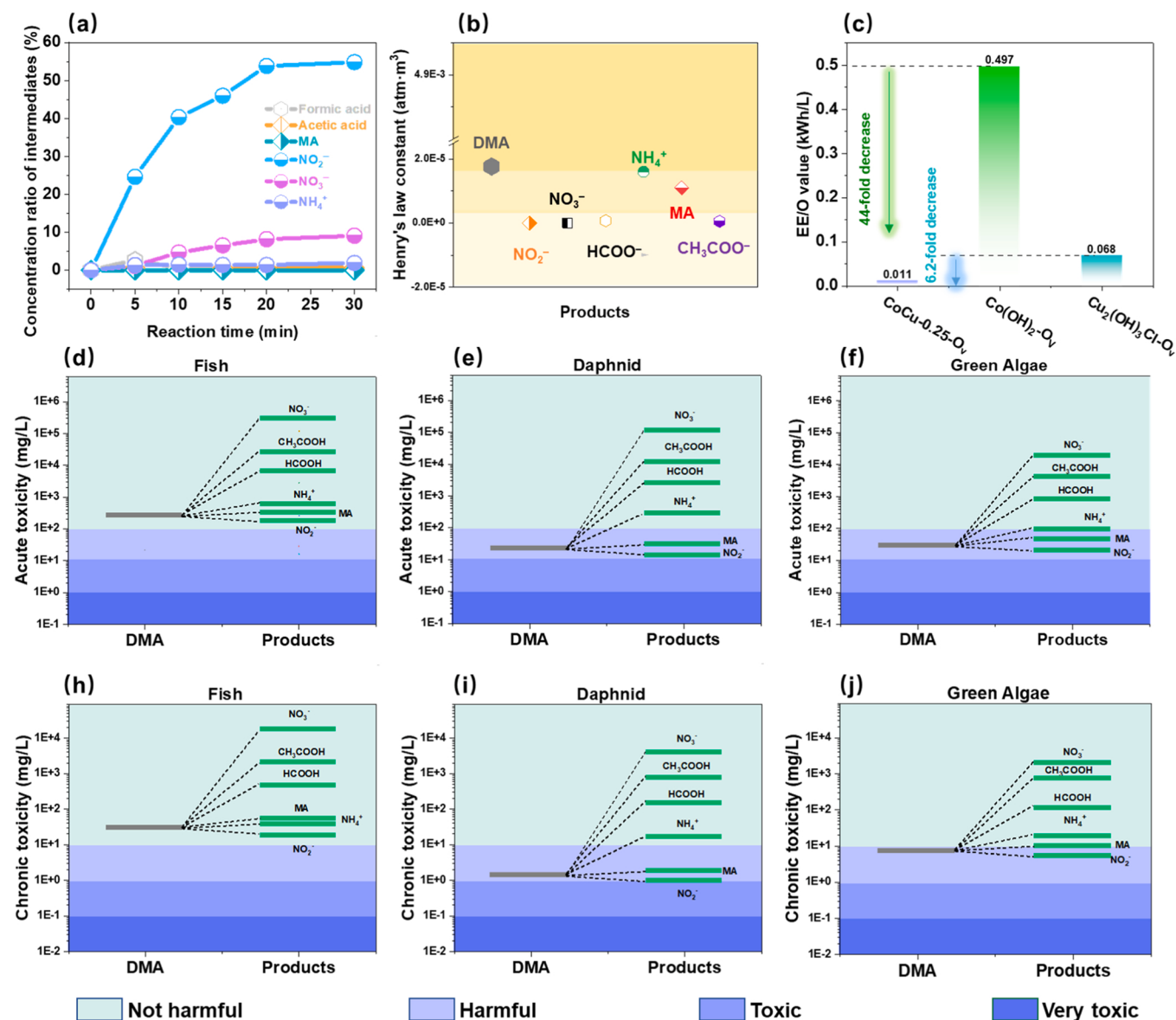


Fig. 7. (a) Products varying with reaction time. (b) Volatility assessment of intermediates of DMA. (c) Economic evaluation. (d-f) Acute toxicity assessment. (h-j) Chronic toxicity assessment.

with ternary $\text{Co}^{\text{III}}\text{O}_v^{\text{IV}}\text{Cu}$ sites that caused by the interactive lattice substitution of non-equivalent metals. Compared with the control groups containing binary sites (i.e., $\text{Co}^{\text{III}}\text{O}_v^{\text{IV}}$ and $\text{Cu}^{\text{III}}\text{O}_v^{\text{IV}}$), it can achieve dual improvements in the removal performance of DMA and PMS utilization rate simultaneously. Multi-scaled *in-situ* characterizations and DFT calculations unveiled that ternary $\text{Co}^{\text{III}}\text{O}_v^{\text{IV}}\text{Cu}$ sites can strengthen the co-adsorption and co-activation of DMA and DO molecules at the interface by pushing up *d*-band center and reducing work function. The reinforced co-activation triggers DMA and DO to replace PMS as electron donor and acceptor for consumption, respectively. Meanwhile, neighboring $\text{Co}^{\text{III}}\text{O}_v^{\text{IV}}\text{Cu}$ sites boost DMA degradation by enhanced multiple pathways (i.e., $^1\text{O}_2$ and $\text{SO}_4^{\text{2-}}$ attacks, and self-oxidation) and shortened migration distance of active species to DMA. As a result, extraordinary dual improvements can be achieved. Through this catalytic process, various amine pollutants are efficiently converted and degraded at a wide pH range (3–12). Moreover, our developed system exhibits a decreasing biotoxicity and volatility process, strong environmental durability, and low treatment cost. This system is of great environmental significance for the treatment of refractory organics in a more green and sustainable way, and could guide the further design of

high-performance and oxidant-saving Fenton-like systems based on synergies between multiple sites to meet industrial demand.

CRediT authorship contribution statement

Qin Dai: Conceptualization, Validation, Data curation, Writing – review & editing. **Guangfei Yu:** Conceptualization, Validation, Data curation, Writing – review & editing. **Juanjuan Qi:** Visualization, Investigation. **Yanan Wang:** Data curation, Investigation. **Yihao Wang:** Data curation, Investigation. **Zhijie Zhang:** Data curation, Investigation. **Xiaolin Zhong:** Data curation, Investigation. **Zhimo Fang:** Data curation, Investigation. **Lei Xing:** Conceptualization, Writing – review & editing. **Penghui Du:** Conceptualization, Writing – review & editing. **Lai Lyu:** Conceptualization, Validation, Writing – review & editing. **Lidong Wang:** Writing – review & editing, Project administration, Funding acquisition, Resources.

Declaration of Competing Interest

The authors declare that they have no known competing financial

interests or personal relationships that could have appeared to influence the work reported in this paper.

Data Availability

Data will be made available on request.

Acknowledgments

This work was financially supported by National Natural Science Foundation of China (No. 52200126, 51878273, and 52122009), Natural Science Foundation of Hebei Province (No. E2019502199). The authors would like to thank ECOSAR software provided by the U.S. Environmental Protection Agency.

Appendix A. Supporting information

Supplementary data associated with this article can be found in the online version at doi:10.1016/j.apcatb.2023.123184.

References

- [1] L. Onel, M. Blitz, M. Dryden, L. Thonger, P. Seakins, Branching ratios in reactions of OH radicals with methylamine, dimethylamine, and ethylamine, *Environ. Sci. Technol.* 48 (2014) 9935–9942.
- [2] S. Biswas, H. Kwon, K.C. Barsanti, N. Myllys, J.N. Smith, B.M. Wong, Ab initio metadynamics calculations of dimethylamine for probing pK_b variations in bulk vs. surface environments, *Phys. Chem. Chem. Phys.* 22 (2020) 26265–26277.
- [3] Q. Dai, Z. Li, X. Zhong, Y. Wang, J. Qi, Y. Wang, Z. Fang, L. Xing, Z. Li, L. Wang, Preventing re-emission of malodorous dimethylamine via tunable nonradical oxidation catalyzed by waste mask-derived carbocatalyst, *Chem. Eng. J.* 450 (2022), 138510.
- [4] J. Lin, Q. Dai, H. Zhao, H. Cao, T. Wang, G. Wang, C. Chen, Photoinduced release of volatile organic compounds from fatty alcohols at the air-water interface: The role of singlet oxygen photosensitized by a carbonyl group, *Environ. Sci. Technol.* 55 (2021) 8683–8690.
- [5] Y. Wang, G. Yang, Y. Lu, Y. Liu, L. Wang, Detection of gaseous dimethylamine using vocus proton-transfer-reaction time-of-flight mass spectrometry, *Atmos. Environ.* 243 (2020), 117875.
- [6] Y. He, H. Cheng, Degradation of N-nitrosodimethylamine (NDMA) and its precursor dimethylamine (DMA) in mineral micropores induced by microwave irradiation, *Water Res.* 94 (2016) 305–314.
- [7] Z.Y. Guo, C.X. Li, M. Gao, X. Han, Y.J. Zhang, W.J. Zhang, W.W. Li, Mn-O covalency governs the intrinsic activity of Co-Mn spinel oxides for boosted peroxymonosulfate activation, *Angew. Chem. Int. Ed. Engl.* 60 (2021) 274–280.
- [8] C. Song, Q. Zhan, F. Liu, C. Wang, H. Li, X. Wang, X. Guo, Y. Cheng, W. Sun, L. Wang, J. Qian, B. Pan, Overturned loading of inert CeO₂ to active Co₃O₄ for unusually improved catalytic activity in Fenton-like reactions, *Angew. Chem. Int. Ed. Engl.* 61 (2022), e202200406.
- [9] P. Shao, J. Tian, F. Yang, X. Duan, S. Gao, W. Shi, X. Luo, F. Cui, S. Luo, S. Wang, Identification and regulation of active sites on nanodiamonds: establishing a highly efficient catalytic system for oxidation of organic contaminants, *Adv. Funct. Mater.* 28 (2018) 1705295.
- [10] Y. Wei, J. Miao, J. Ge, J. Lang, C. Yu, L. Zhang, P.J.J. Alvarez, M. Long, Ultrahigh peroxymonosulfate utilization efficiency over CuO nanosheets via heterogeneous Cu(III) formation and preferential electron transfer during degradation of phenols, *Environ. Sci. Technol.* 56 (2022) 8984–8992.
- [11] J. Lee, U. von Gunten, J.H. Kim, Persulfate-based advanced oxidation: Critical assessment of opportunities and roadblocks, *Environ. Sci. Technol.* 54 (2020) 3064–3081.
- [12] E.T. Yun, H.Y. Yoo, H. Bae, H.I. Kim, J. Lee, Exploring the role of persulfate in the activation process: Radical precursor versus electron acceptor, *Environ. Sci. Technol.* 51 (2017) 10090–10099.
- [13] X. Zhou, M.-K. Ke, G.-X. Huang, C. Chen, W. Chen, K. Liang, Y. Qu, J. Yang, Y. Wang, F. Li, H.-Q. Yu, Y. Wu, Identification of Fenton-like active Cu sites by heteroatom modulation of electronic density, *Proc. Natl. Acad. Sci. USA* 119 (2022), e2119492119.
- [14] J. Ali, L. Wenli, A. Shahzad, J. Ifthikar, G.G. Aregay, I.I. Shahib, Z. Elkhli, Z. Chen, Z. Chen, Regulating the redox centers of Fe through the enrichment of Mo moiety for persulfate activation: a new strategy to achieve maximum persulfate utilization efficiency, *Water Res.* 181 (2020), 115862.
- [15] M. Huang, Y. Han, W. Xiang, D. Zhong, C. Wang, T. Zhou, X. Wu, J. Mao, In situ-formed phenoxyl radical on the CuO surface triggers efficient persulfate activation for phenol degradation, *Environ. Sci. Technol.* 55 (2021) 15361–15370.
- [16] S. Zhan, H. Zhang, X. Mi, Y. Zhao, C. Hu, L. Lyu, Efficient Fenton-like process for pollutant removal in electron-rich/poor reaction sites induced by surface oxygen vacancy over cobalt-zinc oxides, *Environ. Sci. Technol.* 54 (2020) 8333–8343.
- [17] Q. Yan, C. Lian, K. Huang, L. Liang, H. Yu, P. Yin, J. Zhang, M. Xing, Constructing an acidic microenvironment by MoS₂ in heterogeneous Fenton reaction for pollutant control, *Angew. Chem. Int. Ed. Engl.* 60 (2021) 17155–17163.
- [18] X. Mi, H. Zhong, H. Zhang, S. Xu, Y. Li, H. Wang, S. Zhan, J.C. Crittenden, Facilitating redox cycles of copper species by pollutants in peroxymonosulfate activation, *Environ. Sci. Technol.* 56 (2022) 2637–2646.
- [19] H. Li, A. Jie, Jia Zhihui, Zhang Falong, Lizhi, Oxygen vacancy-mediated photocatalysis of bioc: Reactivity, selectivity, and perspectives, *Angew. Chem. Int. Ed. Engl.* 57 (2017) 122–138.
- [20] Z. Zhao, P. Wang, C. Song, T. Zhang, S. Zhan, Y. Li, Enhanced interfacial electron transfer by asymmetric Cu-Ov-Ln sites on Ln₂O₃ for efficient peroxymonosulfate activation, *Angew. Chem. Int. Ed.* 135 (2023), e202216403.
- [21] K. Yu, L.L. Lou, S. Liu, W. Zhou, Asymmetric oxygen vacancies: the intrinsic redox active sites in metal oxide catalysts, *Adv. Sci.* 7 (2019) 1901970.
- [22] Y. Gao, Z. Chen, Y. Zhu, T. Li, C. Hu, New insights into the generation of singlet oxygen in the metal-free peroxymonosulfate activation process: Important role of electron-deficient carbon atoms, *Environ. Sci. Technol.* 54 (2020) 1232–1241.
- [23] T. Ma, R. Jacobs, J. Booske, D. Morgan, Work function trends and new low-work-function boride and nitride materials for electron emission applications, *J. Phys. Chem. C.* 125 (2021) 17400–17410.
- [24] Shan Gao, Yongfu Sun, Fengcai Lei, Liu Liang, Wentuan Jiawei, Ultrahigh energy density realized by a single-layer beta-Co(OH)₂ all-solid-state asymmetric supercapacitor, in: *Angew. Chem. Int. Ed. Engl.* 53, 2014, pp. 12789–12793.
- [25] G. Henkelman, A. Arnaldsson, H. Jónsson, A fast and robust algorithm for bader decomposition of charge density, *Comp. Mater. Sci.* 36 (2006) 354–360.
- [26] Z. Liu, R. Ma, M. Osada, K. Takada, T. Sasaki, Selective and controlled synthesis of α - and β -cobalt hydroxides in highly developed hexagonal platelets, *J. Am. Chem. Soc.* 127 (2005) 13869–13874.
- [27] F. Dionigi, J. Zhu, Z. Zeng, T. Merzdorf, H. Sarodnik, M. Gleich, L. Pan, W.X. Li, J. Greeley, P. Strasser, Intrinsic electrocatalytic activity for oxygen evolution of crystalline 3d-transition metal layered double hydroxides, *Angew. Chem. Int. Ed. Engl.* 60 (2021) 14446–14457.
- [28] L. Gao, F. Bao, X. Tan, M. Li, Z. Shen, X. Chen, Z. Tang, W. Lai, Y. Lu, P. Huang, C. Ma, S.C. Smith, Z. Ye, Z. Hu, H. Huang, Engineering a local potassium cation concentrated microenvironment toward ampere-level current density hydrogen evolution reaction, *Energy Environ. Sci.* 16 (2023) 285–294.
- [29] L. Wu, Z. Sun, Y. Zhen, S. Zhu, C. Yang, J. Lu, Y. Tian, D. Zhong, J. Ma, Oxygen vacancy-induced nonradical degradation of organics: Critical trigger of oxygen (O₂) in the Fe-Co LDH/peroxymonosulfate system, *Environ. Sci. Technol.* 55 (2021) 15400–15411.
- [30] Y. Wang, H. Ji, W. Liu, T. Xue, C. Liu, Y. Zhang, L. Liu, Q. Wang, F. Qi, B. Xu, Novel CuCo₂O₄ composite spinel with a meso-macroporous nanosheet structure for sulfate radical formation and benzophenone-4 degradation: Interface reaction, degradation pathway, and DFT calculation, *ACS Appl. Mater. Interfaces* 12 (2020) 20522–20535.
- [31] W. Cheng, Z.P. Wu, D. Luan, S.Q. Zang, X.W. Lou, Synergetic cobalt-copper-based bimetal-organic framework nanoboxes toward efficient electrochemical oxygen evolution, *Angew. Chem. Int. Ed. Engl.* 60 (2021) 26397–26402.
- [32] C. Pei, M.C. Kim, Y. Li, C. Xia, J. Kim, W. So, X. Yu, H.S. Park, J.K. Kim, Electron transfer-induced metal spin-crossover at NiCo₂Si/ReS₂ 2D–2D interfaces for promoting pH-universal hydrogen evolution reaction, *Adv. Funct. Mater.* 33 (2023) 2210072.
- [33] T. Zhang, Z. Sun, S. Li, B. Wang, Y. Liu, R. Zhang, Z. Zhao, Regulating electron configuration of single Cu sites via unsaturated N₂O-coordination for selective oxidation of benzene, *Nat. Commun.* 13 (2022) 6996.
- [34] M. Li, H. Zhu, Q. Yuan, T. Li, M. Wang, P. Zhang, Y. Zhao, D. Qin, W. Guo, B. Liu, Proximity electronic effect of Ni/Co diatomic sites for synergistic promotion of electrocatalytic oxygen reduction and hydrogen evolution, *Adv. Funct. Mater.* 33 (2023) 2210867.
- [35] Y. Zhou, L. Liu, G. Li, C. Hu, Insights into the influence of ZrO₂ crystal structures on methyl laurate hydrogenation over Co/ZrO₂ catalysts, *ACS Catal.* 11 (2021) 7099–7113.
- [36] W. Bing, L. Zheng, S. He, D. Rao, M. Xu, L. Zheng, B. Wang, Y. Wang, M. Wei, Insights on active sites of CaAl-hydrotalcite as a high-performance solid base catalyst toward aldol condensation, *ACS Catal.* 8 (2017) 656–664.
- [37] Q. Zhang, Y. Huang, S. Peng, T. Huang, J.J. Cao, W. Ho, S. Lee, Synthesis of SrFe_xTi_{1-x}O₃-delta nanocubes with tunable oxygen vacancies for selective and efficient photocatalytic NO oxidation, *Appl. Catal. B* 239 (2018) 1–9.
- [38] F. Ren, H. Li, Y. Wang, J. Yang, Enhanced photocatalytic oxidation of propylene over V-doped TiO₂ photocatalyst: Reaction mechanism between V⁵⁺ and single-electron-trapped oxygen vacancy, *Appl. Catal. B* 176 (2015) 160–172.
- [39] L. Lyu, D. Yan, G. Yu, W. Cao, C. Hu, Efficient destruction of pollutants in water by a dual-reaction-center Fenton-like process over carbon nitride compounds-complexed Cu(II)-CuAlO₂, *Environ. Sci. Technol.* 52 (2018) 4294–4304.
- [40] S. Xu, H. Zhu, W. Cao, Z. Wen, J. Wang, C.P. François-Xavier, T. Wintgens, Cu-Al₂O₃-g-C₃N₄ and Cu-Al₂O₃-C-dots with dual-reaction centres for simultaneous enhancement of Fenton-like catalytic activity and selective H₂O₂ conversion to hydroxyl radicals, *Appl. Catal. B* 234 (2018) 223–233.
- [41] X. Li, X. Huang, S. Xi, S. Miao, J. Ding, W. Cai, S. Liu, X. Yang, H. Yang, J. Gao, Single cobalt atoms anchored on porous N-doped graphene with dual reaction sites for efficient Fenton-like catalysis, *J. Am. Chem. Soc.* 140 (2018) 12469–12475.
- [42] M. El Kateb, C. Trellu, A. Darwich, M. Rivallin, M. Bechelany, S. Nagarajan, S. Lacour, N. Bellakhal, G. Lesage, M. Héran, M. Cretin, Electrochemical advanced oxidation processes using novel electrode materials for mineralization and biodegradability enhancement of nanofiltration concentrate of landfill leachates, *Water Res.* 162 (2019) 446–455.

[43] Y.J. Zhang, G.X. Huang, L.R. Winter, J.J. Chen, L. Tian, S.C. Mei, Z. Zhang, F. Chen, Z.Y. Guo, R. Ji, Y.Z. You, W.W. Li, X.W. Liu, H.Q. Yu, M. Elimelech, Simultaneous nanocatalytic surface activation of pollutants and oxidants for highly efficient water decontamination, *Nat. Commun.* 13 (2022) 3005.

[44] W. An, X. Li, J. Ma, L. Ma, Advanced treatment of industrial wastewater by ozonation with iron-based monolithic catalyst packing: From mechanism to application, *Water Res.* 235 (2023), 119860.

[45] G. Yu, Y. Wu, H. Cao, Q. Ge, Q. Dai, S. Sun, Y. Xie, Insights into the mechanism of ozone activation and singlet oxygen generation on N-doped defective nanocarbons: A DFT and machine learning study, *Environ. Sci. Technol.* 56 (2022) 7853–7863.

[46] Y. Wang, P. Zhang, L. Lyu, T. Li, C. Hu, Preferential destruction of micropollutants in water through a self-purification process with dissolved organic carbon polar complexation, *Environ. Sci. Technol.* 56 (2022) 10849–10856.

[47] J. Qi, X. Yang, P.-Y. Pan, T. Huang, X. Yang, C.-C. Wang, W. Liu, Interface engineering of Co (OH)₂ nanosheets growing on the KNbO₃ perovskite based on electronic structure modulation for enhanced peroxyomonosulfate activation, *Environ. Sci. Technol.* 56 (2022) 5200–5212.

[48] L. Wang, Y. Wang, Z. Wang, P. Du, L. Xing, W. Xu, J. Ni, S. Liu, Y. Wang, G. Yu, Q. Dai, Proton transfer triggered *in-situ* construction of C≡N active site to activate PMS for efficient autocatalytic degradation of low-carbon fatty amine, *Water Res.* 240 (2023), 120119.

[49] Z.Y. Guo, Y. Si, W.Q. Xia, F. Wang, H.Q. Liu, C. Yang, W.J. Zhang, W.W. Li, Electron delocalization triggers nonradical Fenton-like catalysis over spinel oxides, *Proc. Natl. Acad. Sci. USA* 119 (2022), e2201607119.

[50] S. Li, Y. Yang, H. Zheng, Y. Zheng, C.-S. He, B. Lai, J. Ma, J. Nan, Introduction of oxygen vacancy to manganese ferrite by Co substitution for enhanced peracetic acid activation and ¹O₂ dominated tetracycline hydrochloride degradation under microwave irradiation, *Water Res.* 225 (2022), 119176.

[51] M. Yang, K. Wu, S. Sun, J. Duan, X. Liu, J. Cui, S. Liang, Y. Ren, Unprecedented relay catalysis of curved Fe₁–N₄ single-atom site for remarkably efficient ¹O₂ generation, *ACS Catal.* (2022) 681–691.

[52] C. Dong, Y. Bao, T. Sheng, Q. Yi, Q. Zhu, B. Shen, M. Xing, I.M.C. Lo, J. Zhang, Singlet oxygen triggered by robust bimetallic MoFe/TiO₂ nanospheres of highly efficacy in solar-light-driven peroxyomonosulfate activation for organic pollutants removal, *Appl. Catal. B* 286 (2021), 119930.

[53] J. Wang, Y. Xie, G. Yu, L. Yin, J. Xiao, Y. Wang, W. Lv, Z. Sun, J.H. Kim, H. Cao, Manipulating selectivity of hydroxyl radical generation by single-atom catalysts in catalytic ozonation: Surface or solution, *Environ. Sci. Technol.* 56 (2022) 17753–17762.

[54] X. Sun, L. Sun, G. Li, Y. Tuo, C. Ye, J. Yang, J. Low, X. Yu, J.H. Bitter, Y. Lei, D. Wang, Y. Li, Phosphorus tailors the d-band center of copper atomic sites for efficient CO₂ photoreduction under visible-light irradiation, *Angew. Chem. Int. Ed. Engl.* 61 (2022), e202207677.

[55] C. Wang, P. Zhai, M. Xia, W. Liu, J. Gao, L. Sun, J. Hou, Identification of the origin for reconstructed active sites on oxyhydroxide for oxygen evolution reaction, *Adv. Mater.* 35 (2023) 2209307.

[56] Y. Zou, J. Hu, B. Li, L. Lin, Y. Li, F. Liu, X.-Y. Li, Tailoring the coordination environment of cobalt in a single-atom catalyst through phosphorus doping for enhanced activation of peroxyomonosulfate and thus efficient degradation of sulfadiazine, *Appl. Catal. B* 312 (2022), 121408.

[57] B. Zhu, B. Cheng, L. Zhang, J. Yu, Review on DFT calculation of *s*-triazine-based carbon nitride, *Carbon Energy* 1 (2019) 32–56.

[58] L. Xie, P. Wang, Y. Li, D. Zhang, D. Shang, W. Zheng, Y. Xia, S. Zhan, W. Hu, Pauling-type adsorption of O₂ induced electrocatalytic singlet oxygen production on N-CuO for organic pollutants degradation, *Nat. Commun.* 13 (2022) 1–11.

[59] C. Fan, X. Wang, X. Wu, Y. Chen, Z. Wang, M. Li, D. Sun, Y. Tang, G. Fu, Neodymium-evoked valence electronic modulation to balance reversible oxygen electrocatalysis, *Adv. Energy Mater.* 13 (2023) 2203244.

[60] Y. Zhou, Y. Gao, S.Y. Pang, J. Jiang, Y. Yang, J. Ma, Y. Yang, J. Duan, Q. Guo, Oxidation of fluoroquinolone antibiotics by peroxyomonosulfate without activation: Kinetics, products, and antibacterial deactivation, *Water Res.* 145 (2018) 210–219.

[61] Y. Shang, H. Ning, J. Shi, Y. Wu, S.N. Luo, Effects of anharmonicity, recrossing, tunneling, and pressure on the H-abstractions from dimethylamine by triplets O and O₂, *J. Phys. Chem. A* 126 (2022) 825–833.

[62] A.P. Bhat, P.R. Gogate, Degradation of nitrogen-containing hazardous compounds using advanced oxidation processes: a review on aliphatic and aromatic amines, dyes, and pesticides, *J. Hazard. Mater.* 403 (2021), 123657.

[63] P. Shao, S. Yu, X. Duan, L. Yang, H. Shi, L. Ding, J. Tian, L. Yang, X. Luo, S. Wang, Potential difference driving electron transfer via defective carbon nanotubes toward selective oxidation of organic micropollutants, *Environ. Sci. Technol.* 54 (2020) 8464–8472.

[64] H. Yao, P. Sun, D. Minakata, J.C. Crittenden, C.H. Huang, Kinetics and modeling of degradation of ionophore antibiotics by UV and UV/H₂O₂, *Environ. Sci. Technol.* 47 (2013) 4581–4589.